expressing beta(2)-adrenergic receptors in the heart. *Cardiovasc Res* 48: 448–454, 2000.

12. **Dyachok O, Isakov Y, Sagetorp J, Tengholm A.** Oscillations of cyclic AMP in hormone-stimulated insulin-secreting beta-cells. *Nature* 439: 349–352, 2006.
13. **Efendiev R, Dessauer CW.** A kinase-anchoring proteins and adenylyl cyclase in cardiovascular physiology and pathology. *J Cardiovasc Pharmacol* 58: 339–344, 2011.
14. **Elkayam U, Tasissa G, Binanay C, Stevenson LW, Gheorghiade M, Warnica JW, Young JB, Rayburn BK, Rogers JG, DeMarco T, Leier CV.** Use and impact of inotropes and vasodilator therapy in hospitalized patients with severe heart failure. *Am Heart J* 153: 98–104, 2007.
15. **Engelhardt S, Hein L, Dyachenkow V, Kranias EG, Isenberg G, Lohse MJ.** Altered calcium handling is critically involved in the cardiotoxic effects of chronic beta-adrenergic stimulation. *Circulation* 109: 1154–1160, 2004.
16. **Engelhardt S, Hein L, Wiesmann F, Lohse MJ.** Progressive hypertrophy and heart failure in beta1-adrenergic receptor transgenic mice. *Proc Natl Acad Sci USA* 96: 7059–7064, 1999.
17. **Esposito G, Perrino C, Ozaki T, Takaoka H, Defer N, Petretta MP, De Angelis MC, Mao L, Hanoune J, Rockman HA, Chiariello M.** Increased myocardial contractility and enhanced exercise function in transgenic mice overexpressing either adenylyl cyclase 5 or 8. *Basic Res Cardiol* 103: 22–30, 2008.
18. **Fang CX, Dong F, Thomas DP, Ma H, He L, Ren J.** Hypertrophic cardiomyopathy in high-fat diet-induced obesity: role of suppression of forkhead transcription factor and atrophy gene transcription. *Am J Physiol Heart Circ Physiol* 295: H1206–H1215, 2008.
19. **Feldman AM.** Adenylyl cyclase: a new target for heart failure therapeutics. *Circulation* 105: 1876–1878, 2002.
20. **Fujino T, Hasebe N, Kawabe J, Fujita M, Fukuzawa J, Tobise K, Kikuchi K.** Effect of beta-adrenoceptor antagonist and angiotensin-converting enzyme inhibitor on hypertension-associated changes in adenylyl cyclase type V messenger RNA expression in spontaneously hypertensive rats. *J Cardiovasc Pharmacol* 41: 720–725, 2003.
21. **Georget M, Mateo P, Vandecasteele G, Jurevicius J, Lipskaia L, Defer N, Hanoune J, Hoerter J, Fischmeister R.** Augmentation of cardiac contractility with no change in L-type Ca^{2+} current in transgenic mice with a cardiac-directed expression of the human adenylyl cyclase type 8 (AC8). *FASEB J* 16: 1636–1638, 2002.
22. **Gerhardstein BL, Puri TS, Chien AJ, Hosey MM.** Identification of the sites phosphorylated by cyclic AMP-dependent protein kinase on the beta 2 subunit of L-type voltage-dependent calcium channels. *Biochemistry* 38: 10361–10370, 1999.
23. **Gottle M, Geduhn J, Konig B, Gille A, Hocherl K, Seifert R.** Characterization of mouse heart adenylyl cyclase. *J Pharmacol Exp Ther* 329: 1156–1165, 2009.
24. **Gresl TA, Colman RJ, Roecker EB, Havighurst TC, Huang Z, Allison DB, Bergman RN, Kemnitz JW.** Dietary restriction and glucose regulation in aging rhesus monkeys: a follow-up report at 8.5 yr. *Am J Physiol Endocrinol Metab* 281: E757–E765, 2001.
25. **Gros R, Ding Q, Chorazyczewski J, Pickering JG, Limbird LE, Feldman RD.** Adenylyl cyclase isoform-selective regulation of vascular smooth muscle proliferation and cytoskeletal reorganization. *Circ Res* 99: 845–852, 2006.
26. **Grossman W, Jones D, McLaurin LP.** Wall stress and patterns of hypertrophy in the human left ventricle. *J Clin Invest* 56: 56–64, 1975.
27. **Guellich A, Gao S, Hong C, Yan L, Wagner TE, Dhar SK, Ghaleb B, Hittinger L, Iwatsubo K, Ishikawa Y, Vatner SF, Vatner DE.** Effects of cardiac overexpression of type 6 adenylyl cyclase affects on the response to chronic pressure overload. *Am J Physiol Heart Circ Physiol* 299: H707–H712, 2010.
28. **Haber N, Stengel D, Defer N, Roeckel N, Mattei MG, Hanoune J.** Chromosomal mapping of human adenylyl cyclase genes type III, type V and type VI. *Hum Genet* 94: 69–73, 1994.
29. **Hakonarson H, Grunstein MM.** Regulation of second messengers associated with airway smooth muscle contraction and relaxation. *Am J Respir Crit Care Med* 158: S115–S122, 1998.
30. **Hjalmarson A, Goldstein S, Fagerberg B, Wedel H, Waagstein F, Kjekshus J, Wikstrand J, El Allaf D, Vitovec J, Aldershvile J, Halinen M, Dietz R, Neuhaus KL, Janosi A, Thorgeirsson G, Dunselman PH, Gullestad L, Kuch J, Herlitz J, Rickenbacher P, Ball S, Gottlieb S, Deedwania P.** Effects of controlled-release metoprolol on total mortality, hospitalizations, and well-being in patients with heart failure: the Metoprolol CR/XL Randomized Intervention Trial in congestive heart failure (MERIT-HF). MERIT-HF Study Group. *JAMA* 283: 1295–1302, 2000.
31. **Ho D, Yan L, Iwatsubo K, Vatner DE, Vatner SF.** Modulation of beta-adrenergic receptor signaling in heart failure and longevity: targeting adenylyl cyclase type 5. *Heart Fail Rev* 15: 495–512, 2010.
32. **Ho D, Yan L, Zhao X, Bravo C, Stanley W, Vatner DE, Pessin J, Vatner SF.** Disruption of adenylyl cyclase type 5, a novel target for obesity, diabetes and diabetic cardiomyopathy (Abstract). *Circulation* 126: A19323 2012.
33. **Hu CL, Chandra R, Ge H, Pain J, Yan L, Babu G, Depre C, Iwatsubo K, Ishikawa Y, Sadoshima J, Vatner SF, Vatner DE.** Adenylyl cyclase type 5 protein expression during cardiac development and stress. *Am J Physiol Heart Circ Physiol* 297: H1776–H1782, 2009.
34. **Iancu RV, Jones SW, Harvey RD.** Compartmentation of cAMP signaling in cardiac myocytes: a computational study. *Biophys J* 92: 3317–3331, 2007.
35. **Ishikawa Y, Katsushika S, Chen L, Halnon NJ, Kawabe J, Homcy CJ.** Isolation and characterization of a novel cardiac adenylylcyclase cDNA. *J Biol Chem* 267: 13553–13557, 1992.
36. **Iwase M, Bishop SP, Uechi M, Vatner DE, Shannon RP, Kudej RK, Wight DC, Wagner TE, Ishikawa Y, Homcy CJ, Vatner SF.** Adverse effects of chronic endogenous sympathetic drive induced by cardiac GS alpha overexpression. *Circ Res* 78: 517–524, 1996.
37. **Iwase M, Uechi M, Vatner DE, Asai K, Shannon RP, Kudej RK, Wagner TE, Wight DC, Patrick TA, Ishikawa Y, Homcy CJ, Vatner SF.** Cardiomyopathy induced by cardiac Gsα overexpression. *Am J Physiol Heart Circ Physiol* 272: H585–H589, 1997.
38. **Iwatsubo K, Bravo C, Uechi M, Baljinnyam E, Nakamura T, Umemura M, Lai L, Gao S, Yan L, Zhao X, Park M, Qiu H, Okumura S, Iwatsubo M, Vatner DE, Vatner SF, Ishikawa Y.** Prevention of heart failure in mice by an antiviral agent that inhibits type 5 cardiac adenylyl cyclase. *Am J Physiol Heart Circ Physiol* 302: H2622–H2628, 2012.
39. **Kapiloff MS, Piggott LA, Sadana R, Li J, Heredia LA, Henson E, Efendiev R, Dessauer CW.** An adenylyl cyclase-mAKAPbeta signaling complex regulates cAMP levels in cardiac myocytes. *J Biol Chem* 284: 23540–23546, 2009.
40. **Koren MJ, Devereux RB, Casale PN, Savage DD, Laragh JH.** Relation of left ventricular mass and geometry to morbidity and mortality in uncomplicated essential hypertension. *Ann Intern Med* 114: 345–352, 1991.
41. **Lai L, Yan L, Gao S, Hu CL, Ge H, Davidow A, Park M, Bravo C, Iwatsubo K, Ishikawa Y, Auwerx J, Sinclair DA, Vatner SF, Vatner DE.** Type 5 adenylyl cyclases increases oxidative stress by transcriptional regulation of MnSOD via the SIRT1/FoxO3a pathway. *Circulation* 127: 1692–1701, 2013.
42. **Lakatta EG.** Age-associated cardiovascular changes in health: impact on cardiovascular disease in older persons. *Heart Fail Rev* 7: 29–49, 2002.
43. **Lakatta EG.** Arterial and cardiac aging: major shareholders in cardiovascular disease enterprises: Part III: cellular and molecular clues to heart and arterial aging. *Circulation* 107: 490–497, 2003.
44. **Lambertz H, Meyer J, Erbel R.** Long-term hemodynamic effects of prenalterol in patients with severe congestive heart failure. *Circulation* 69: 298–305, 1984.
45. **Lee GJ, Yan L, Vater DE, Vatner SF.** β-Adrenergic receptor signaling in heart failure. In: *Cardiac Remodeling: Molecular Mechanisms,* edited by Jugdutt BI and Dhalla NS. New York: Springer, 2013.
46. **Liggett SB, Tepe NM, Lorenz JN, Canning AM, Jantz TD, Mitarai S, Yatani A, Dorn GW, 2nd.** Early and delayed consequences of beta(2)-adrenergic receptor overexpression in mouse hearts: critical role for expression level. *Circulation* 101: 1707–1714, 2000.
47. **Lohse MJ, Engelhardt S, Eschenhagen T.** What is the role of beta-adrenergic signaling in heart failure? *Circ Res* 93: 896–906, 2003.
48. **Marx SO, Reiken S, Hisamatsu Y, Jayaraman T, Burkhoff D, Rosemblit N, Marks AR.** PKA phosphorylation dissociates FKBP12.6 from the calcium release channel (ryanodine receptor): defective regulation in failing hearts. *Cell* 101: 365–376, 2000.
49. **Matsui Y, Takagi H, Qu X, Abdellatif M, Sakoda H, Asano T, Levine B, Sadoshima J.** Distinct roles of autophagy in the heart during ischemia and reperfusion: roles of AMP-activated protein kinase and Beclin 1 in mediating autophagy. *Circ Res* 100: 914–922, 2007.
50. **Mattison JA, Roth GS, Beasley TM, Tilmont EM, Handy AM, Herbert RL, Longo DL, Allison DB, Young JE, Bryant M, Barnard D, Ward WF, Qi W, Ingram DK, de Cabo R.** Impact of caloric restriction

on health and survival in rhesus monkeys from the NIA study. *Nature* 489: 318–321, 2012.

51. **Milano CA, Allen LF, Rockman HA, Dolber PC, McMinn TR, Chien KR, Johnson TD, Bond RA, Lefkowitz RJ.** Enhanced myocardial function in transgenic mice overexpressing the beta 2-adrenergic receptor. *Science* 264: 582–586, 1994.
52. **Mons N, Guillou JL, Jaffard R.** The role of Ca^{2+}/calmodulin-stimulable adenylyl cyclases as molecular coincidence detectors in memory formation. *Cell Mol Life Sci* 55: 525–533, 1999.
53. **Muller G, Wied S, Over S, Frick W.** Inhibition of lipolysis by palmitate, H_2O_2 and the sulfonylurea drug, glimepiride, in rat adipocytes depends on cAMP degradation by lipid droplets. *Biochemistry* 47: 1259–1273, 2008.
54. **Neves MJ, Terenzi HF.** In vivo control of gluconeogenesis in wild-type Neurospora crassa and in the adenylate cyclase-deficient cr-1 (crisp) mutant. *J Bacteriol* 171: 1767–1771, 1989.
55. **O'Connor CM, Gattis WA, Uretsky BF, Adams KF Jr, McNulty SE, Grossman SH, McKenna WJ, Zannad F, Swedberg K, Gheorghiade M, Califf RM.** Continuous intravenous dobutamine is associated with an increased risk of death in patients with advanced heart failure: insights from the Flolan International Randomized Survival Trial (FIRST). *Am Heart J* 138: 78–86, 1999.
56. **Okumura S, Suzuki S, Ishikawa Y.** New aspects for the treatment of cardiac diseases based on the diversity of functional controls on cardiac muscles: effects of targeted disruption of the type 5 adenylyl cyclase gene. *J Pharm Sci* 109: 354–359, 2009.
57. **Okumura S, Takagi G, Kawabe J, Yang G, Lee MC, Hong C, Liu J, Vatner DE, Sadoshima J, Vatner SF, Ishikawa Y.** Disruption of type 5 adenylyl cyclase gene preserves cardiac function against pressure overload. *Proc Natl Acad Sci USA* 100: 9986–9990, 2003.
58. **Okumura S, Vatner DE, Kurotani R, Bai Y, Gao S, Yuan Z, Iwatsubo K, Ulucan C, Kawabe J, Ghosh K, Vatner SF, Ishikawa Y.** Disruption of type 5 adenylyl cyclase enhances desensitization of cyclic adenosine monophosphate signal and increases Akt signal with chronic catecholamine stress. *Circulation* 116: 1776–1783, 2007.
59. **Ostrom RS, Naugle JE, Hase M, Gregorian C, Swaney JS, Insel PA, Brunton LL, Meszaros JG.** Angiotensin II enhances adenylyl cyclase signaling via Ca^{2+}/calmodulin. Gq-Gs cross-talk regulates collagen production in cardiac fibroblasts. *J Biol Chem* 278: 24461–24468, 2003.
60. **Packer M, Bristow MR, Cohn JN, Colucci WS, Fowler MB, Gilbert EM, Shusterman NH.** The effect of carvedilol on morbidity and mortality in patients with chronic heart failure. US Carvedilol Heart Failure Study Group. *N Engl J Med* 334: 1349–1355, 1996.
61. **Park M, Park J, Lee J, Tian B, Lai L, Iwatsubo K, Ishikawa Y, Sadoshima J, Vatner DE, Vatner SF.** Cardiac overexpression of adenylyl cyclase type 5 induces left ventricular hypertrophy potentially by activating calcineurin-NFAT signaling (Abstract). *FASEB J* 365–311, 2011.
62. **Park SY, Cho YR, Kim HJ, Higashimori T, Danton C, Lee MK, Dey A, Rothermel B, Kim YB, Kalinowski A, Russell KS, Kim JK.** Unraveling the temporal pattern of diet-induced insulin resistance in individual organs and cardiac dysfunction in C57BL/6 mice. *Diabetes* 54: 3530–3540, 2005.
63. **Peter PS, Brady JE, Yan L, Chen W, Engelhardt S, Wang Y, Sadoshima J, Vatner SF, Vatner DE.** Inhibition of p38 alpha MAPK rescues cardiomyopathy induced by overexpressed beta 2-adrenergic receptor, but not beta 1-adrenergic receptor. *J Clin Invest* 117: 1335–1343, 2007.
64. **Petrashevskaya N, Gaume BR, Mihlbachler KA, Dorn GW, 2nd, Liggett SB.** Bitransgenesis with beta(2)-adrenergic receptors or adenylyl cyclase fails to improve beta(1)-adrenergic receptor cardiomyopathy. *Clin Transl Sci* 1: 221–227, 2008.
65. **Rengo G, Zincarelli C, Femminella GD, Liccardo D, Pagano G, de Lucia C, Altobelli GG, Cimini V, Ruggiero D, Perrone-Filardi P, Gao E, Ferrara N, Lymperopoulos A, Koch WJ, Leosco D.** Myocardial beta(2)-adrenoceptor gene delivery promotes coordinated cardiac adaptive remodelling and angiogenesis in heart failure. *Br J Pharmacol* 166: 2348–2361, 2012.
66. **Rosenberg D, Groussin L, Bertagna X, Bertherat. J.** cAMP pathway alterations from the cell surface to the nucleus in adrenocortical tumors. *Endocr Res* 28: 765–775, 2002.
67. **Sadana R, Dessauer CW.** Physiological roles for G protein-regulated adenylyl cyclase isoforms: insights from knockout and overexpression studies. *Neurosignals* 17: 5–22, 2009.
68. **Segev A, Mekori YA.** The Cardiac Insufficiency Bisoprolol Study II. *Lancet* 353: 1361, 1999.
69. **Shah RS, Lee HG, Xiongwei Z, Perry G, Smith MA, Castellani RJ.** Current approaches in the treatment of Alzheimer's disease. *Biomed Pharmacother* 62: 199–207, 2008.
70. **Simmerman HK, Jones LR.** Phospholamban: protein structure, mechanism of action, and role in cardiac function. *Physiol Rev* 78: 921–947, 1998.
71. **Sinclair DA.** Toward a unified theory of caloric restriction and longevity regulation. *Mech Ageing Dev* 126: 987–1002, 2005.
72. **Sulakhe PV, Vo XT.** Regulation of phospholamban and troponin-I phosphorylation in the intact rat cardiomyocytes by adrenergic and cholinergic stimuli: roles of cyclic nucleotides, calcium, protein kinases and phosphatases and depolarization. *Mol Cell Biochem* 149–150: 103–126, 1995.
73. **Sutherland EW, Rall TW.** Fractionation and characterization of a cyclic adenine ribonucleotide formed by tissue particles. *J Biol Chem* 232: 1077–1091, 1958.
74. **Tepe NM, Liggett SB.** Transgenic replacement of type V adenylyl cyclase identifies a critical mechanism of beta-adrenergic receptor dysfunction in the G alpha q overexpressing mouse. *FEBS Lett* 458: 236–240, 1999.
75. **Tesmer JJ, Sunahara RK, Gilman AG, Sprang SR.** Crystal structure of the catalytic domains of adenylyl cyclase in a complex with Gsalpha. GTPgammaS. *Science* 278: 1907–1916, 1997.
76. **Tevaearai HT, Eckhart AD, Walton GB, Keys JR, Wilson K, Koch WJ.** Myocardial gene transfer and overexpression of beta2-adrenergic receptors potentiates the functional recovery of unloaded failing hearts. *Circulation* 106: 124–129, 2002.
77. **Timofeyev V, Porter CA, Tuteja D, Qiu H, Li N, Tang T, Singapuri A, Han PL, Lopez JE, Hammond HK, Chiamvimonvat N.** Disruption of adenylyl cyclase type V does not rescue the phenotype of cardiac-specific overexpression of Galphaq protein-induced cardiomyopathy. *Am J Physiol Heart Circ Physiol* 299: H1459–H1467, 2010.
78. **Vatner DE, Sato N, Ishikawa Y, Kiuchi K, Shannon RP, Vatner SF.** Beta-adrenoceptor desensitization during the development of canine pacing-induced heart failure. *Clin Exp Pharmacol Physiol* 23: 688–692, 1996.
79. **Vatner SF, Vatner DE, Yan L.** Models of longevity (calorie restriction and AC5 KO): result of three bad hypotheses. *Aging (Albany NY)* 4: 662–663, 2012.
80. **Weiss EP, Racette SB, Villareal DT, Fontana L, Steger-May K, Schechtman KB, Klein S, Holloszy JO.** Improvements in glucose tolerance and insulin action induced by increasing energy expenditure or decreasing energy intake: a randomized controlled trial. *Am J Clin Nutr* 84: 1033–1042, 2006.
81. **Wilkins BJ, Dai YS, Bueno OF, Parsons SA, Xu J, Plank DM, Jones F, Kimball TR, Molkentin JD.** Calcineurin/NFAT coupling participates in pathological, but not physiological, cardiac hypertrophy. *Circ Res* 94: 110–118, 2004.
82. **Willoughby D, Cooper DM.** Organization and Ca^{2+} regulation of adenylyl cyclases in cAMP microdomains. *Physiol Rev* 87: 965–1010, 2007.
83. **Willoughby D, Wachten S, Masada N, Cooper DM.** Direct demonstration of discrete Ca^{2+} microdomains associated with different isoforms of adenylyl cyclase. *J Cell Sci* 123: 107–117, 2010.
84. **Yan L, Park JY, Dillinger JG, De Lorenzo MS, Yuan C, Lai L, Wang C, Ho D, Tian B, Stanley WC, Auwerx J, Vatner DE, Vatner SF.** Common mechanisms for calorie restriction and adenylyl cyclase type 5 knockout models of longevity. *Aging Cell* 11: 1110–1120, 2012.
85. **Yan L, Vatner DE, O'Connor JP, Ivessa A, Ge H, Chen W, Hirotani S, Ishikawa Y, Sadoshima J, Vatner SF.** Type 5 adenylyl cyclase disruption increases longevity and protects against stress. *Cell* 130: 247–258, 2007.
86. **Zaccolo M, Pozzan T.** Discrete microdomains with high concentration of cAMP in stimulated rat neonatal cardiac myocytes. *Science* 295: 1711–1715, 2002.
87. **Zhang G, Liu Y, Ruoho AE, Hurley JH.** Structure of the adenylyl cyclase catalytic core. *Nature* 386: 247–253, 1997.

Available online at www.sciencedirect.com

SciVerse ScienceDirect

British Journal of Oral and Maxillofacial Surgery 51 (2013) e26–e28

BRITISH Journal of Oral and Maxillofacial Surgery

www.bjoms.com

Technical note

Sentinel lymph node biopsy using a new indocyanine green fluorescence imaging system with a colour charged couple device camera for oral cancer

Toshinori Iwai [a,*], Jiro Maegawa [b], Makoto Hirota [a], Iwai Tohnai [a]

[a] *Department of Oral and Maxillofacial Surgery, Yokohama City University Graduate School of Medicine, 3-9 Fukuura, Kanazawa-ku, Yokohama, Kanagawa 236-0004, Japan*

[b] *Department of Plastic and Reconstructive Surgery, Yokohama City University Hospital, 3-9 Fukuura, Kanazawa-ku, Yokohama, Kanagawa 236-0004, Japan*

Accepted 5 March 2012

Available online 26 March 2012

Keywords: Sentinel lymph node biopsy; Indocyanine green; Indocyanine green fluorescence imaging system; Oral cancer; N0

Whether management of N0 neck in patients with oral cancer should be by observation or prophylactic neck dissection is controversial, as 20–30% of patients have occult cervical lymph node metastases.[1] Accurate diagnosis of any metastasis is difficult despite the various imaging methods available, and consequently sentinel lymph node biopsy using blue dye, or a radioisotope, or both, has been used for these patients.[1,2] However, biopsy is associated with several problems, including poor transcutaneous identification of the sentinel lymph nodes, high cost, the shine-through phenomenon, and exposure to radiation. Cost-effective indocyanine green (ICG) without radiation exposure has recently been used to detect sentinel nodes in patients with various cancers.[3,4] Although ICG fluorescence imaging systems have advantages over conventional methods, identifying soft tissues such as muscles or nerves around the nodes is challenging on the monochromatic images produced. This requires surgeons to biopsy sentinel nodes under direct visualisation while also referring to the monochromatic images on the monitor. We report the use of a new ICG fluorescence imaging system that uses a colour charged couple device (CCD) camera for sentinel node biopsy in patients with oral cancer and will overcome these problems.

Preoperative computed tomographic lymphography was used to map the nodes three-dimensionally. To detect them intraoperatively we used the HyperEye Medical System (HEMS; Mizuho Ikakogyo Co., Ltd., Tokyo, Japan), which can visualise ICG-enhanced structures in vivid colour. An arm-type HEMS (USD 150,000) and a hand-type HEMS (USD 100,000) are available (Figs. 1 and 2). First, the mucosal surgical margin was marked with diathermy or laser in case with the mucosa changed colour after the injection. At each of 4 points around the oral lesion 20 mg/4 ml ICG 0.5–1 ml (Diagnogreen 0.5%; Daiichi Pharmaceutical, Tokyo, Japan) was injected. Several seconds later, the subcutaneous nodes could be seen transcutaneously with colour fluorescence imaging using the HEMS, because the ICG fluorescence can penetrate up to 1.5–2.0 cm.[2] A skin incision 2–3 cm long was then made along the proposed incision line of the neck dissection. After incision of the skin and platysma muscle, the sentinel node could be biopsied easily, as it could be clearly identified under colour fluorescence imaging (Figs. 3 and 4). Although ICG-fluorescing nodes cannot always be detected transcutaneously if they are deep in the subcutaneous

* Corresponding author. Tel.: +81 45 787 2659; fax: +81 45 785 8438.
E-mail address: iwai104oams@yahoo.co.jp (T. Iwai).

doi:10.1016/j.bjoms.2012.03.002

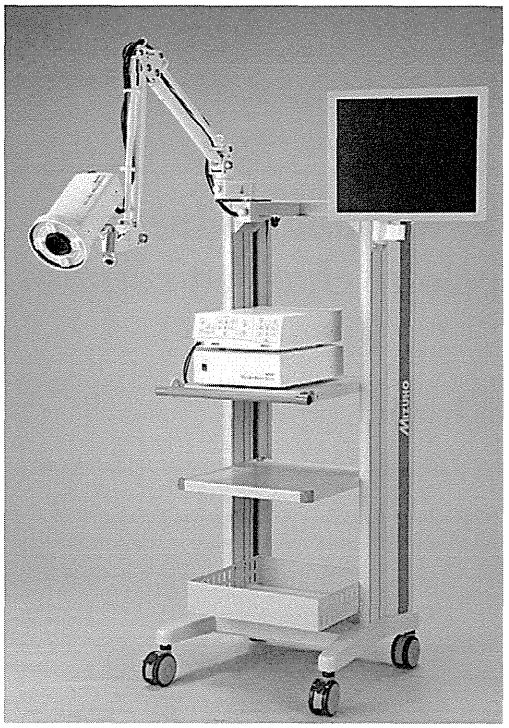

Fig. 1. Arm-type indocyanine green fluorescence imaging system: the HyperEye Medical System.

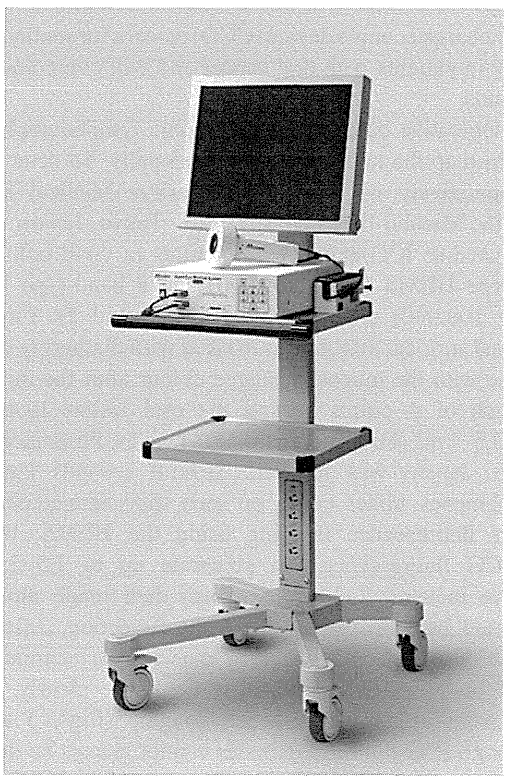

Fig. 2. Hand-type indocyanine green fluorescence imaging system: the HyperEye Medical System.

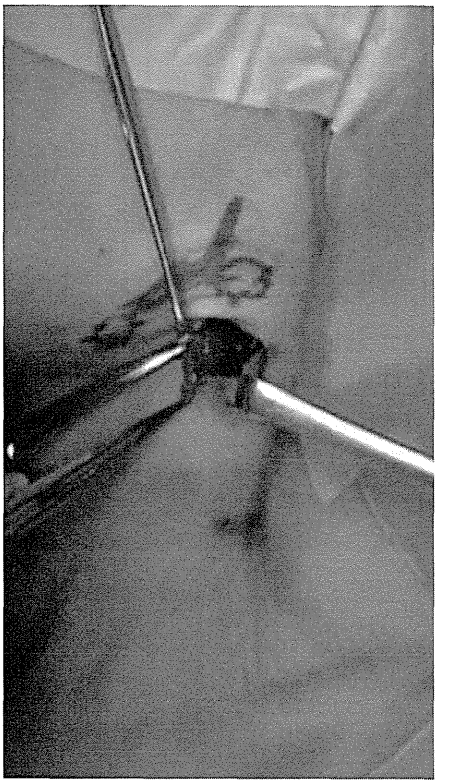

Fig. 3. Intraoperative view of sentinel lymph node biopsy.

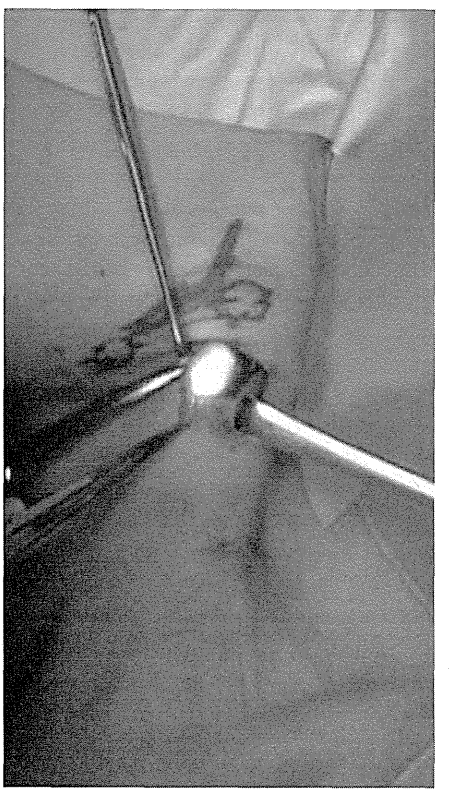

Fig. 4. Colour and near-infrared images of sentinel lymph node biopsy.

tissue, nodes can be biopsied using ICG in such cases by mapping them preoperatively and then making the skin incision.

We biopsied sentinel nodes using the HEMS as described by Yamauchi et al.[2] who showed the feasibility of the technique in animal models. As HEMS can simultaneously capture colour and near-infrared images, surgeons can easily identify surrounding anatomical structures such as nerves, vessels, and muscles as well as the nodes, because they are shown in vivid colour in the operative field. This new method has potential, but should be used in conjunction with radioisotopes until the problem of limited penetration of the fluorescence has been resolved by further study, and the accuracy of identification of subcutaneous nodes has been improved.

References

1. Stoeckli SJ, Alkureishi LW, Ross GL. Sentinel node biopsy for early oral and oraopharyngeal squamous cell carcinoma. *Eur Arch Otorhinolaryngol* 2009;**266**:787–93.
2. Yamauchi K, Nagafuji H, Nakamura T, Sato T, Kohno N. Feasibility of ICG fluorescence-guided sentinel node biopsy in animal models using the HyperEye Medical System. *Ann Surg Oncol* 2011;**18**: 2042–7.
3. Bredell MG. Sentinel lymph node mapping by indocyanine green fluorescence imaging in oropharyngeal cancer—preliminary experience. *Head Neck Oncol* 2010;**2**:31.
4. Murawa D, Hirche C, Dresel S, Hünerbein M. Sentinel lymph node biopsy in breast cancer guided by indocyanine green fluorescence. *Br J Surg* 2009;**96**:1289–94.

TRIPLE-PHASE HELICAL COMPUTED TOMOGRAPHY IN DOGS WITH HEPATIC MASSES

KENJI KUTARA, MAMIKO SEKI, CHIEKO ISHIKAWA, MANABU SAKAI, YUMIKO KAGAWA, GENTOKU IIDA, KUMIKO ISHIGAKI, KENJI TESHIMA, KAZUYA EDAMURA, TOMOHIRO NAKAYAMA, KAZUSHI ASANO

The purpose of this study was to determine the utility of triple-phase helical computed tomography (CT) for differentiating canine hepatic masses. Seventy dogs with hepatic masses underwent triple-phase CT followed by surgical removal of the hepatic masses. Triple-phase helical CT scans for each dog included precontrast, arterial phase, portal venous phase, and delayed phase studies. The removed hepatic masses were histopathologically classified as hepatocellular carcinoma ($n = 47$), nodular hyperplasia ($n = 14$), and hepatic metastatic tumors ($n = 9$) in dogs. Of the 47 hepatocellular carcinomas, the most common CT findings included a heterogeneous pattern with hyper-, iso-, and hypoenhancement in both the arterial and portal venous phases (40/47, 85.1%). Of the 14 nodular hyperplasias, the most common CT findings were a homogeneous pattern with hyper- and isoenhancement in both the portal venous and delayed phases (13/14, 92.9%). Of nine hepatic metastatic tumors, the most common CT findings included a homogeneous hypoenhancement pattern in both the arterial and portal venous phases (8/9, 88.9%). In addition, 5 (55.6%) showed homogeneous hypoenhancement patterns in the delayed phase. Findings from our study indicated that triple-phase CT is a useful tool for preoperative differentiation of hepatocellular carcinoma, nodular hyperplasia, and hepatic metastatic tumors in dogs.

Key words: computed tomography, dog, hepatic metastatic tumor, hepatocellular carcinoma, nodular hyperplasia.

Introduction

HELICAL COMPUTED TOMOGRAPHY (CT) allows images of the entire liver to be obtained during the phase of maximum parenchymal enhancement, enabling optimal detection of focal hepatic lesions.[1] Accurate diagnosis is critical in patients with hepatocellular carcinoma (HCC), hepatic metastatic tumors, or nodular hyperplasia (NH) because they are possible candidates for surgical treatment and the tumors have radically different prognoses.[2] Dynamic CT may be useful for distinguishing between benign and malignant neoplasms in humans[3,4] and dogs.[5,6]

Development of multidetector helical CT (MDCT) ensured that dynamic CT could be used to evaluate the hemodynamics of hepatic masses and that triple-phase helical CT could be used to rapidly scan the whole abdomen in three phases. In triple-phase helical CT, a single bolus injection facilitates imaging during the phase of preferential arterial enhancement, that is, the arterial phase, followed by the portal venous phase and delayed phase.[7] In humans, previous studies have shown that triple-phase helical CT improves the detection of various hepatic masses.[7–10] In addition, three-dimensional (3D) reconstruction of triple-phase helical CT would be useful for preoperative planning.[11]

To the best of our knowledge, however, there have been no reports on the triple-phase CT characteristics of for various hepatic masses in dogs. We believe that, as in humans, triple-phase helical CT is a convenient and less invasive method for the differential diagnosis of hepatic masses and preoperative planning in dogs. The purpose of this study was to characterize triple-phase helical CT findings in dogs with naturally occurring hepatocellular carcinoma, nodular hyperplasia, and hepatic metastatic tumors.

Materials and Methods

Animals

Privately owned dogs referred to the Animal Medical Center of Nihon University for suspected hepatic masses were prospectively recruited. For all dogs, suspected hepatic masses were based on abdominal radiography and ultrasonography (US) findings. With informed owner consent,

From the Department of Veterinary Medicine, College of Bioresource Sciences, Nihon University, Fujisawa, Kanagawa, Japan (Kutara, Seki, Ishikawa, Sakai, Iida, Ishigaki, Teshima, Edamura, Nakayama, Asano) and North Labo, Sapporo, Hokkaido, Japan (Kagawa).

Address correspondence and reprint requests to Kazushi Asano, Department of Veterinary Medicine, College of Bioresource Sciences, Nihon University, 1866 Kameino, Fujisawa, Kanagawa 252–0880, Japan. E-mail: asano.kazushi@nihon-u.ac.jp

Received June 1, 2012; accepted for publication June 19, 2013.
doi: 10.1111/vru.12099

the dogs underwent triple-phase helical CT, followed by surgical removal of the hepatic masses. The resected masses were histopathologically diagnosed by Hematoxylin-Eosin staining by one pathologist (Y. K.). The cases with hepatic masses diagnosed as hepatocellular carcinoma, nodular hyperplasia, and hepatic metastatic tumors were selected for image analysis.

Triple-Phase Helical CT technique

In all dogs, an 18–27 G over-the-needle catheter was placed in the cephalic vein. Each dog was premedicated with midazolam hydrochloride (0.2 mg/kg, intravenously) and butorphanol tartrate (0.2 mg/kg, intravenously) and intubated after induction with intravenous propofol. General anesthesia was maintained by mechanical ventilation with isoflurane (1.5–2%) and oxygen (2 l/min). All dogs were positioned in ventral recumbency, and all scans were obtained on a 16 MDCT scanner (Aquilion 16; Toshiba Medical Systems, Otawara, Japan). The scanning parameters were as follows: rotation time, 0.5 s; slice thickness, 1–2 mm; reconstruction interval, 0.5–1 mm; table speed, 16–32 mm/rotation; helical pitch, 16.0; X-ray tube potential, 120 kV; and X-ray tube current, 150 mA. All helical scans were started at the tip of the wing of the ilium in a cranial direction and covered the entire liver. Iohexol (Ioverin 300; Teva Pharma Japan Inc., Nagoya, Japan) was used as a contrast medium and was administered at a dose of 2.5 ml/kg (750 mgI/kg) via the cephalic vein with a power injector (Auto Enhance A-60; Nemoto-Kyorindo, Tokyo, Japan). The injection time was 15–20 s (injection speed, 0.3–3 ml/s) as described previously.[5,12] In cases where the injection speed was calculated to exceed 3 ml/s the injection time of the contrast medium would have to be within 20 s, and so the injection speed was fixed at 3 ml/s (the range of injection time was 21–31 s). Precontrast (before the injection of contrast medium), arterial phase (20 s after the start of injection of the contrast medium), portal venous phase (40 s after the start of the injection), and delayed phase (120 s after the start of the injection) scans were obtained. The scanning time for each phase was approximately 8 s. In all dogs, 3D images were reconstructed from the obtained images on a workstation after scanning (AZE Virtual Place Plus; AZE, Tokyo, Japan).

Image Analysis

All CT images were reviewed on a dedicated computer workstation. The size (largest transverse dimension) and location of the lesion were recorded. The contrast values were recorded as Hounsfield Units (HU). The contrast value of mass enhancement was measured using the most visually enhanced portion of the mass. In cases with two or more masses, the largest tumor was analyzed. For comparative purposes, the contrast values in three portions of the normal hepatic parenchyma adjacent to the mass were measured, and the mean value was calculated as the contrast value of hepatic parenchyma. An attempt was made to maintain a region-of-interest (ROI) area of approximately 30 mm^2 for all measurements of contrast values. Hyperenhancement was defined as a mass contrast value at least 10 HU greater than the hepatic parenchyma contrast value. Isoenhancement was defined as a mass contrast value was that was greater or less than the hepatic parenchyma contrast value by <10 HU, and hypoenhancement was defined as a mass contrast value at least 10 HU less than the hepatic parenchyma contrast value. Further, each lesion was judged to have homogeneous or heterogeneous enhancement in each phase as described previously.[2] Homogeneous and heterogeneous lesions were scored as being hypo-, iso-, or hyperenhanced.

Data Analysis

Statistical tests were performed using commercially available statistical analysis software (Stat Mate III; ATMs. Co, Tokyo, Japan). Data on the hepatic mass and parenchyma contrast values, body weight, mass size, and injection time and speed were represented as mean ± standard deviation. Spearman's rank test was used to analyze relationships among all of the contrast values and body weight, mass size, and the injection time and speed of the contrast medium. The Mann–Whitney *U*-test was used to compare hepatic parenchyma and mass contrast values. The contrast enhancement patterns were analyzed by a Chi-square test, followed by Yates post hoc correction test. Body weight, injection speed, the size and number of masses, and the contrast values were statistically compared for all mass types using the Kruskal–Wallis *H*-test. The relationship between mass size and contrast-enhancement pattern was also analyzed using the Kruskal–Wallis *H*-test. A *P* value less than 0.05 was considered to indicate a statistically significant difference.

Results

A total of 70 dogs were included in the study. Of the 70 dogs (30 males and 40 females; age, 7–16 years) with hepatic masses, 47, 14, and 9 dogs, were diagnosed with hepatocellular carcinoma, nodular hyperplasia, and hepatic metastatic masses, respectively. The nine metastatic masses were derived from seven splenic hemangiosarcomas, one splenic melanoma, and one intestinal undifferentiated sarcoma. The breeds were as follows: 12 mongrels, 10 Shih Tzus, 8 Golden Retrievers, 5 Beagles, 5 Miniature Dachshunds, 5 Shibas, 4 Labrador Retrievers, 4 Shetland Sheepdogs, 3 Chihuahuas, 2 Maltese dogs, 2

TABLE 1. Mean Contrast Values of Hepatic Masses and Surrounding Liver Parenchyma as Seen in 70 Patients on Triple-Phase CT

		AP		PVP		DP	
Type	*n*	Mass	Parenchyma	Mass	Parenchyma	Mass	Parenchyma
Total	70	100.3 ± 38.8	93.9 ± 20.7	123.0 ± 43.1	137.9 ± 15.9	106.3 ± 30.1†	121.7 ± 11.8
HCC	47	102.7 ± 40.3	94.0 ± 21.3	120.9 ± 43.6†	138.9 ± 16.2	104.6 ± 30.3†	122.2 ± 9.4
NH	14	111.6 ± 30.3‡*	90.4 ± 17.5	155.6 ± 25.7*	137.2 ± 18.2	126.2 ± 16.6	122.1 ± 15.3
Metastatic tumor	9	65.6 ± 20.9†	94.4 ± 21.0	83.2 ± 24.8†**	133.8 ± 11.6	84.4 ± 31.1†**	119.4 ± 17.9

The contrast value is the Hounsfield Unit (HU). All data are mean ± SD.
*AP, arterial phase; DP, delayed phase; HCC, hepatocellular carcinoma; NH, nodular hyperplasia; PVP, portal venous phase, †HU of masses were significantly lower than that of liver parenchyma, ‡HU of masses were significantly higher than that of liver parenchyma, *HU of masses were significantly higher than that of the other masses, **HU of masses were significantly lower than that of the other masses.

Pembroke Welsh Corgis, 2 Siberian Huskies, 2 Yorkshire Terriers, 1 American Cocker Spaniel, 1 Border Collie, 1 Flat-coated Retriever, 1 Pointer, 1 Pomeranian, and 1 Toy Poodle. The mean body weight of the dogs was 14.8 ± 9.1 kg, and the mean mass size (largest axial dimension) was 63.5 ± 33.2 mm. The mean size (largest axial dimension) of the hepatocellular carcinoma, nodular hyperplasia, and hepatic metastatic tumor masses was 75.7 ± 26.0, 47.0 ± 31.9, and 20.2 ± 20.4 mm, respectively. The injection speed was 2.0 ± 1.0 ml/s in all dogs. There was no statistical difference in weight/injection speed among mass types. The mean number of hepatocellular carcinoma, nodular hyperplasia, and hepatic metastatic tumor masses was 1.44 ± 0.9 (range: 1–5), 1.57 ± 0.75 (range: 1–3), and 4.77 ± 5.66 (range: 1–16), respectively. As for metastatic tumors, three dogs had more than five masses, whereas six patients had 1–3 masses. The number of hepatic masses was not significantly different among mass types.

The contrast values of the hepatic masses and parenchyma in each phase are summarized in Table 1. For all dogs, the contrast values of the hepatic masses and parenchyma were 100.3 ± 38.8 and 93.9 ± 20.7 HU in the arterial phase, 123.0 ± 43.1 and 137.9 ± 15.9 HU in the portal venous phase, and 106.3 ± 30.1 and 121.7 ± 11.8 HU in the delayed phase, respectively. None of the contrast values was significantly correlated with body weight, mass size, or injection speed. For the hepatocellular carcinomas, the contrast values of the hepatic masses were significantly lower than those of the parenchyma in the portal venous and delayed phases. For the hepatic nodular hyperplasias, the contrast values of the hepatic masses were significantly higher than those of the parenchyma in the arterial phase. For the hepatic metastatic tumors, the contrast values of the hepatic masses were significantly lower than those of the parenchyma in all phases. Moreover, the contrast values of hepatic metastatic tumors were significantly lower than those of the other masses in the arterial and portal venous phases. The contrast values of the hepatic nodular hyperplasias were significantly higher than those of the other masses in the portal venous and delayed phases.

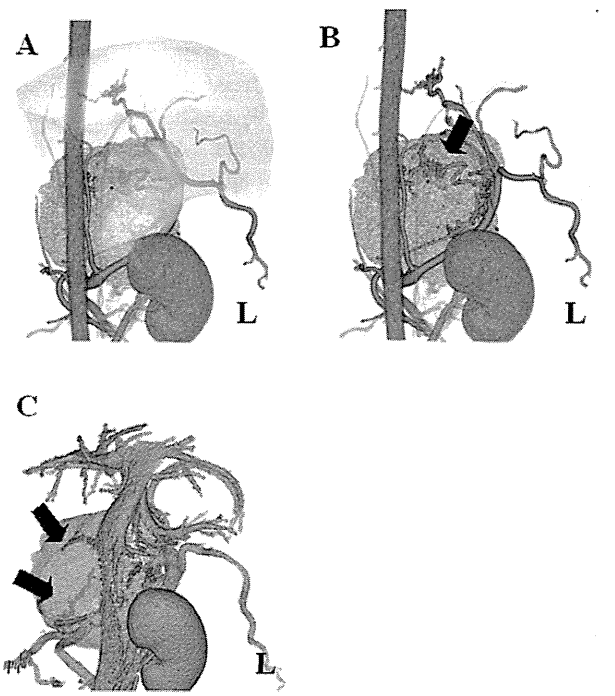

FIG. 1. Three-dimensional (3D) images created using triple phase CT in a dog with hepatocellular carcinoma. The imaging angle is the left dorsal direction. (A) Three-dimensional image in the arterial phase. The brown portion is the liver parenchyma. The green portion is the tumor and the red portion is the aorta and left kidney. Hepatic carcinoma originated from the caudate and right lateral lobes. (B) Three-dimensional image with the liver parenchyma removed in the arterial phase. Arrow: vessel involved in the tumor. (C) Three-dimensional image in the portal venous phase. The blue portions are the veins and left kidney. The purple portion is the portal vein. Arrow: vessel involved in the tumor.

Three-dimensional reconstruction images were created for all dogs. The 3D images were helpful for visualizing the spatial relationships among the masses, liver parenchyma, and intra-abdominal vessels, including the caudal vena cava, portal vein, and hepatic artery and vein (Fig. 1). The contrast-enhancement patterns of all of the hepatic masses are summarized in Table 2. For the hepatocellular carcinomas, the most common contrast-enhancement pattern was heterogeneous enhancement in the arterial phase (85.1%), portal venous phase (85.1%), and delayed

TABLE 2. Enhancement Features of Hepatic Masses as Seen in 70 Patients on Triple-phase CT

		Enhancement pattern		AP		PVP		DP	
Type	*n*	Contrast	Enhancement	*n*	%	*n*	%	*n*	%
HCC	47	Homogeneous		7	14.9	7	14.9	16	34
			Hyper	3	6.4	1	2.1	4	8.5
			Iso	0	0	1	2.1	6	12.8
			Hypo	4	8.5	5	10.6	6	12.8
		Heterogeneous		40†	85.1	40†	85.1	31†	66
			Hyper	21†	44.7	8	17.1	3	6.4
			Iso	9†	19.1	13†	27.6	12†	25.5
			Hypo	10†	21.3	19†	40.4	16†	34
NH	14	Homogeneous		8†	57.1	13†	92.9	13†	92.9
			Hyper	6†	42.9	8†	57.2	3	21.5
			Iso	2†	14.3	5†	35.7	10†	71.4
			Hypo	0	0	0	0	0	0
		Heterogeneous		6	42.9	1	7.1	1	7.1
			Hyper	4	28.6	1	7.1	1	7.1
			Iso	0	0	0	0	0	0
			Hypo	2	14.2	0	0	0	0
Metastasic tumor	9	Homogeneous		9†	100	9†	100	9†	100
			Hyper	0	0	0	0	0	0
			Iso	0	0	1	11.1	4	44.4
			Hypo	9†	100	8†	88.9	5†	55.6
		Heterogeneous		0	0	0	0	0	0
			Hyper	0	0	0	0	0	0
			Iso	0	0	0	0	0	0
			Hypo	0	0	0	0	0	0

AP, arterial phase; DP, delayed phase; HCC, hepatocellular carcinoma; NH, nodular hyperplasia; PVP, portal venous phase. †significantly larger compared with the other groups.

phase (66%) (Fig. 2), which was significantly different compared with those of the other masses. For the hepatic nodular hyperplasias, the most common contrast-enhancement pattern was homogeneous hyper- and isoenhancement in the arterial phase (57.1%), portal venous phase (92.9%), and delayed phase (92.9%; Figs. 3 and 4), which was also significantly different compared with the other masses. For hepatic metastatic tumors, the most common contrast-enhancement pattern was homogeneous hypoenhancement in the arterial phase (100%) and portal venous phase (88.9%). In addition, a homogeneous pattern was seen in all phases, and hypoenhancement was observed in 100% of the arterial phase images and 88.9% of the portal venous phase images. As for the delayed phase images, 44.4% and 55.6%, respectively, showed iso- and hypoenhancement (Figs. 5 and 6). For the metastatic tumors, the most common contrast-enhancement pattern was significantly different from that of the other masses. There was no significant association between contrast-enhancement pattern and mass size.

Discussion

In the current study, body weight and the injection speed were found to have no significant correlations with any of the hepatic parenchyma and mass contrast values. The entire liver was evaluated in one examination with triple-phase helical CT and multiple masses were detected. Three-dimensional reconstruction images showing the detailed morphological features of the canine intra-abdominal structures were also obtained. In addition, the 3D reconstruction imaging techniques helped to identify vascular involvement. A previous study reported that evaluation of enhancement patterns in dynamic CT may be helpful in the differentiation of hepatocellular carcinoma and hepatic nodular hyperplasia in dogs.[5,6] However, in dynamic CT, hepatic masses must be first detected in the precontrast images because the ROI is placed on a predetermined slice for the dynamic scan. In the case of multiple hepatic masses, multiple dynamic scans are required to evaluate the enhancement of different masses. Other previous studies have reported differentiation of hepatic tumors using contrast enhanced US,[13–15] and identified a high diagnostic yield for hepatic masses. However, the field of view for acquiring contrast enhanced US images must be limited to a small focal area and this area must be subjectively selected by the operator.

In our study, CT findings of hepatocellular carcinoma were typically heterogeneous in the arterial and portal venous phases in dogs. In a previous study performed using dual-phase helical CT (arterial and portal venous phases) in human subjects, the most common enhancement pattern in hepatocellular carcinoma was heterogeneous in the

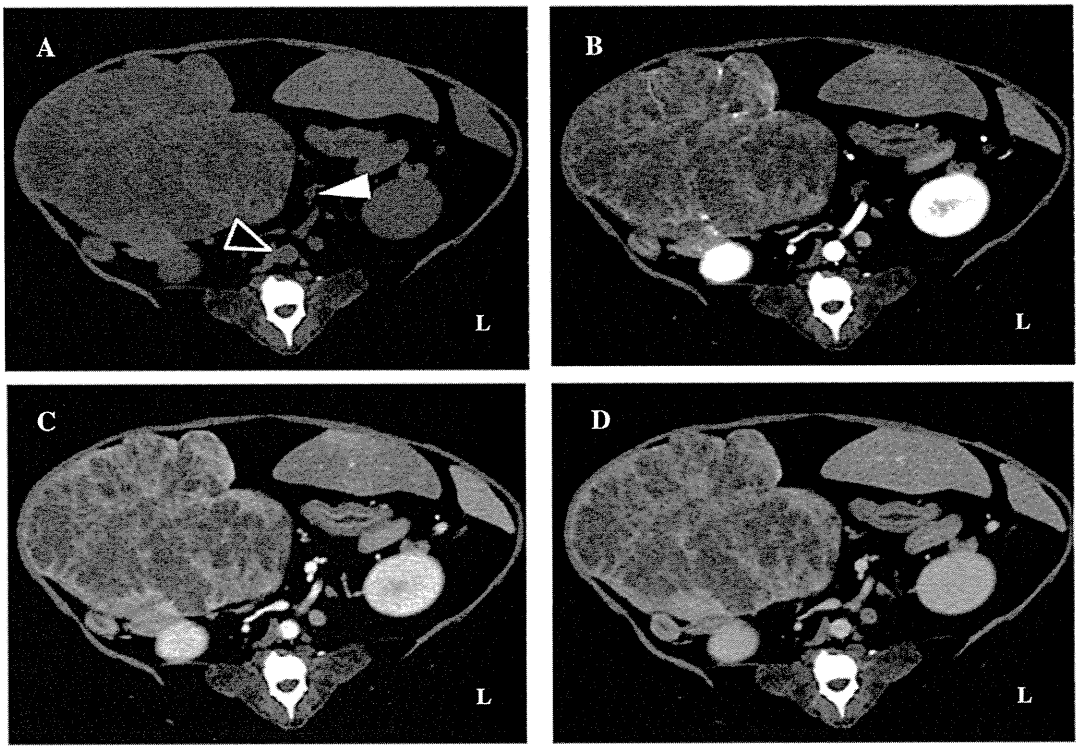

FIG. 2. Triple phase CT characteristics in a dog with hepatocellular carcinoma. (A) Transverse precontrast CT image showing a tumor in the right lobe. (B) Heterogeneous tumor enhancement in the arterial phase. (C) Heterogeneous enhancement in the portal venous phase. (D) Heterogeneous enhancement in the delayed phase. Black arrow head: aorta. White arrow head: portal vein.

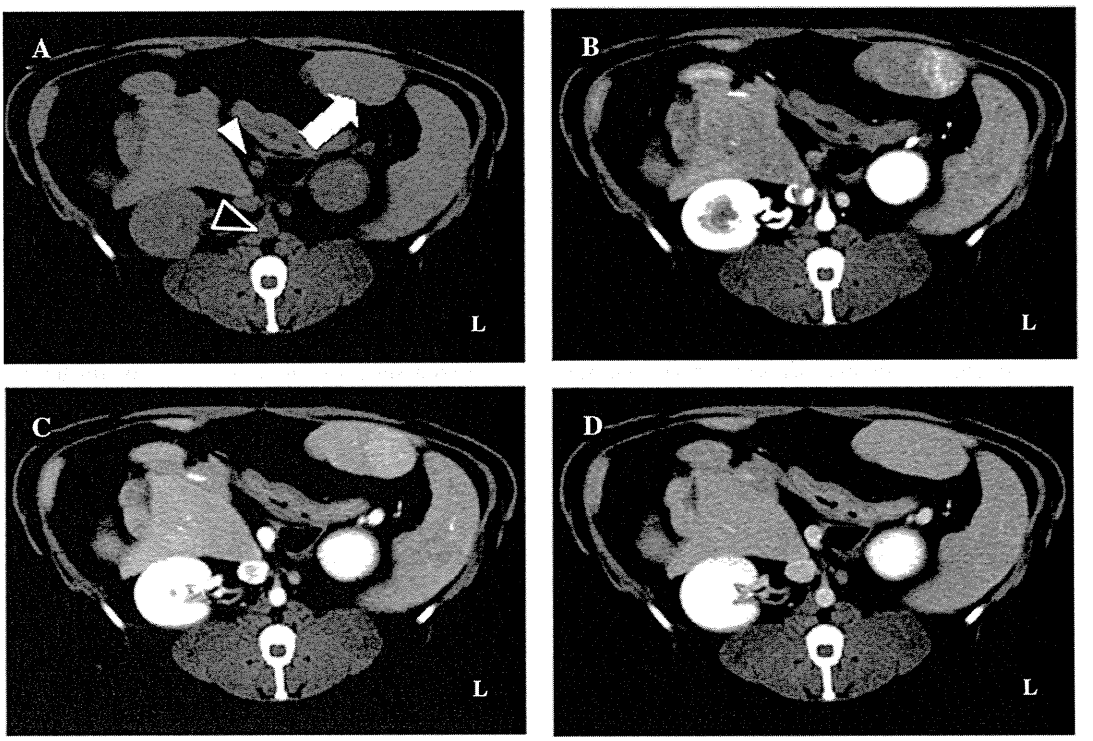

FIG. 3. Triple phase CT characteristics in a dog with nodular hyperplasia. (A) Transverse precontrast CT image showing a mass in the left lobe (arrow). (B) Heterogeneous enhancement in the arterial phase. (C) Homogeneous hyperenhancement in the portal venous phase. (D) Homogeneous isoenhancement in the delayed phase. White arrow: mass. Black arrow head: aorta. White arrow head portal vein.

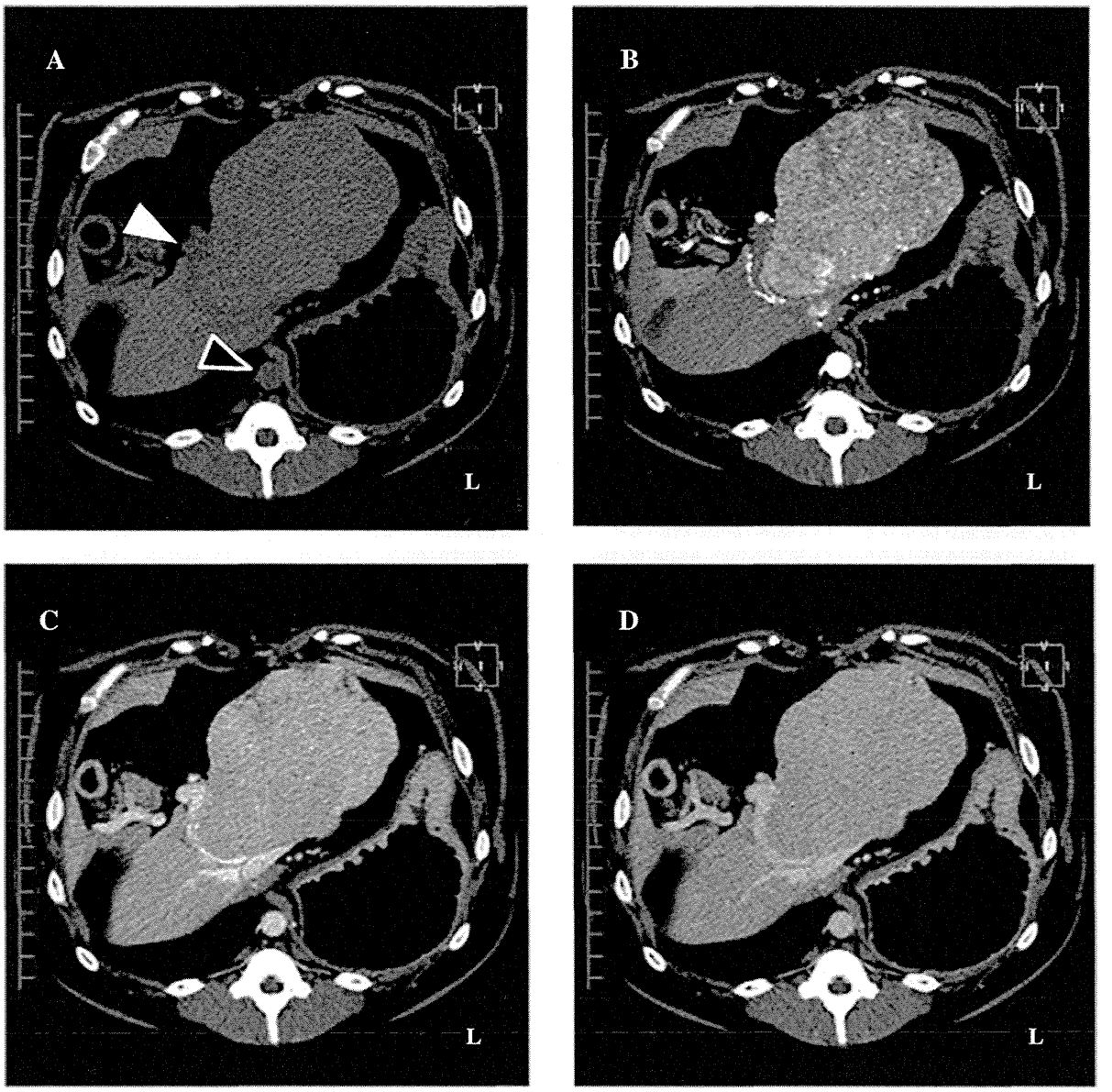

FIG. 4. Triple phase CT characteristics in a dog with nodular hyperplasia. (A) Transverse precontrast CT image showing a mass in the right lobe. (B) Heterogeneous enhancement in the arterial phase. (C) Homogeneous isoenhancement in the portal venous phase. (D) Homogeneous isoenhancement in the delayed phase. Black arrow head: aorta. White arrow head: portal vein.

arterial phase (sensitivity, 60%; specificity, 96%; PPV, 75%)[2] but masses were not identifiable on the portal venous phase images. In dogs with hepatocellular carcinoma, the heterogeneous contrast pattern observed in our study was similar to that observed in previous studies using dynamic CT.[5,6] In these studies,[5,6] hepatocellular carcinoma showed hypoenhancement in the delayed phase. In our study, the average contrast value of the hepatocellular carcinoma was lower than that of the liver parenchyma in the delayed phase. However, just 46% (22/46) of hepatocellular carcinomas showed hypoenhancement in the delayed phase, and the enhancement patterns of hepatocellular carcinoma were comparatively variable. Therefore, evaluation of enhancement based on HU alone risks a misleading differential diagnosis of hepatocellular carcinoma in dogs. CT imaging criteria for hepatocellular carcinoma in humans are based exclusively on the vascular-dynamic findings of hepatocellular carcinoma with Iohexol. A typical enhancement is defined as an early arterial uptake followed by washout in the portal venous or late, delayed phase.[16] In humans, the enhancement pattern of hepatocellular carcinoma is affected by mass size and cellular differentiation.[16–18] In our study,

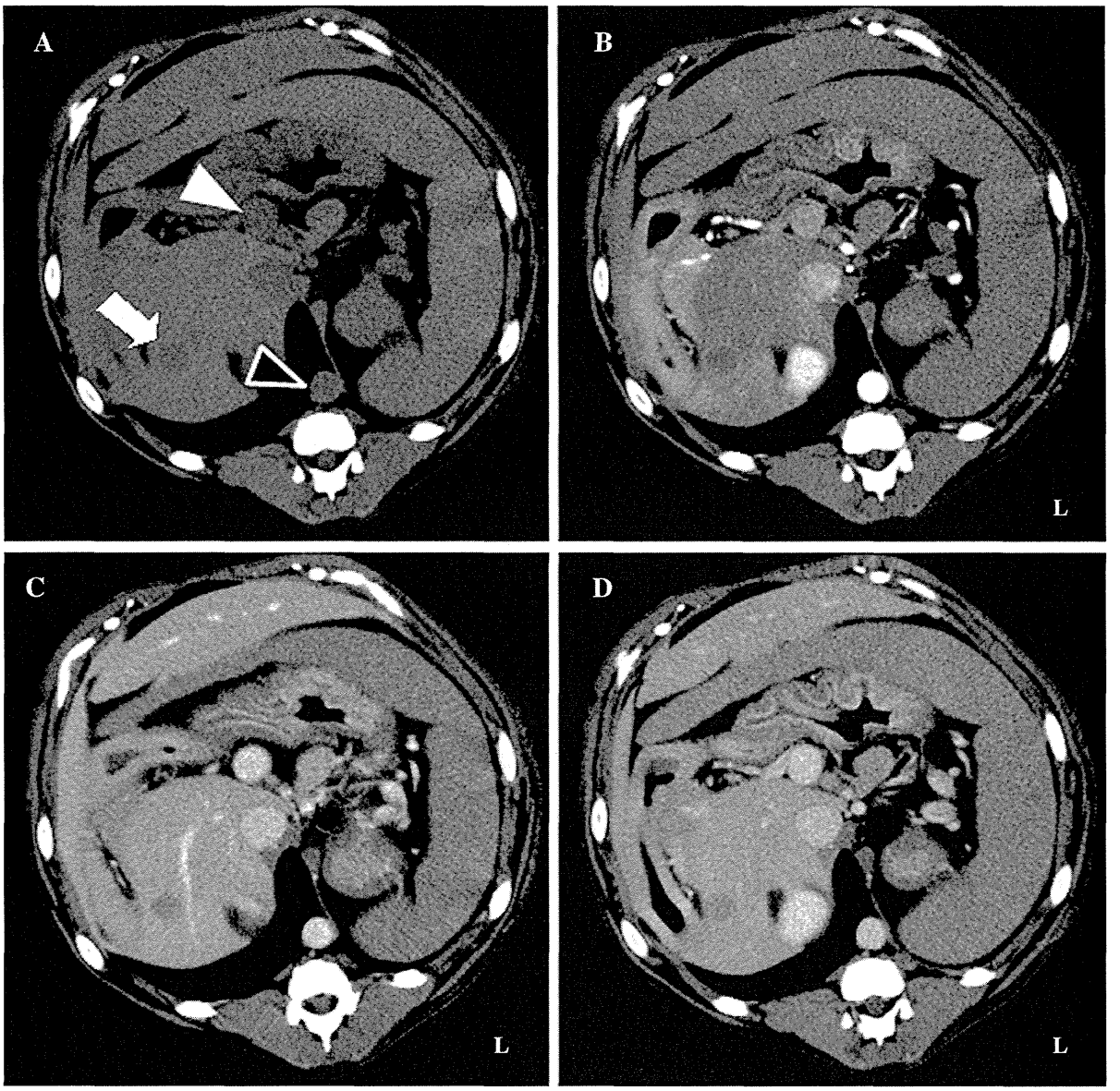

FIG. 5. Triple phase CT characteristics in a dog with a hepatic metastatic tumor. (A) Transverse precontrast CT image showing a mass in the right lobe (arrow). (B) Homogeneous tumor hypoenhancement in the arterial phase. (C) Homogeneous hypoenhancement in the portal venous phase. (D) Homogeneous hypoenhancement in the delayed phase. White arrow: tumor. Black arrow head: aorta. White arrow head: portal vein.

however, the characteristic CT findings of hepatocellular carcinoma were not affected by multiphase enhancement or by tumor size. It is suggested that the vascular dynamics of hepatocellular carcinoma in dogs differs from that in humans. In our study, cellular differentiation and angiogenesis of hepatocellular carcinoma were not investigated. Clarification of the association between pathological changes and contrast-enhancement patterns may be required.

The most common CT findings for dogs with nodular hyperplasia in the present study were a homogeneous pattern and hyper- and isoenhancement in the portal venous and delayed phases. The finding of hyper- and isoenhancement of hepatic nodular hyperplasia in our study is similar to that reported in a previous study,[5] but different from the findings of another study where only isoenhancement in hepatic nodular hyperplasia was reported in dogs.[6] In a dual-phase helical CT study of human subjects, the most common enhancement pattern in nodular hyperplasia was homogeneous hyperenhancement in the portal venous phase (sensitivity, 70%; specificity, 88%; PPV, 61%) and homogeneous isoenhancement in the portal venous phase (sensitivity, 40%; specificity, 96%; PPV, 73%).[2] It is suggested that

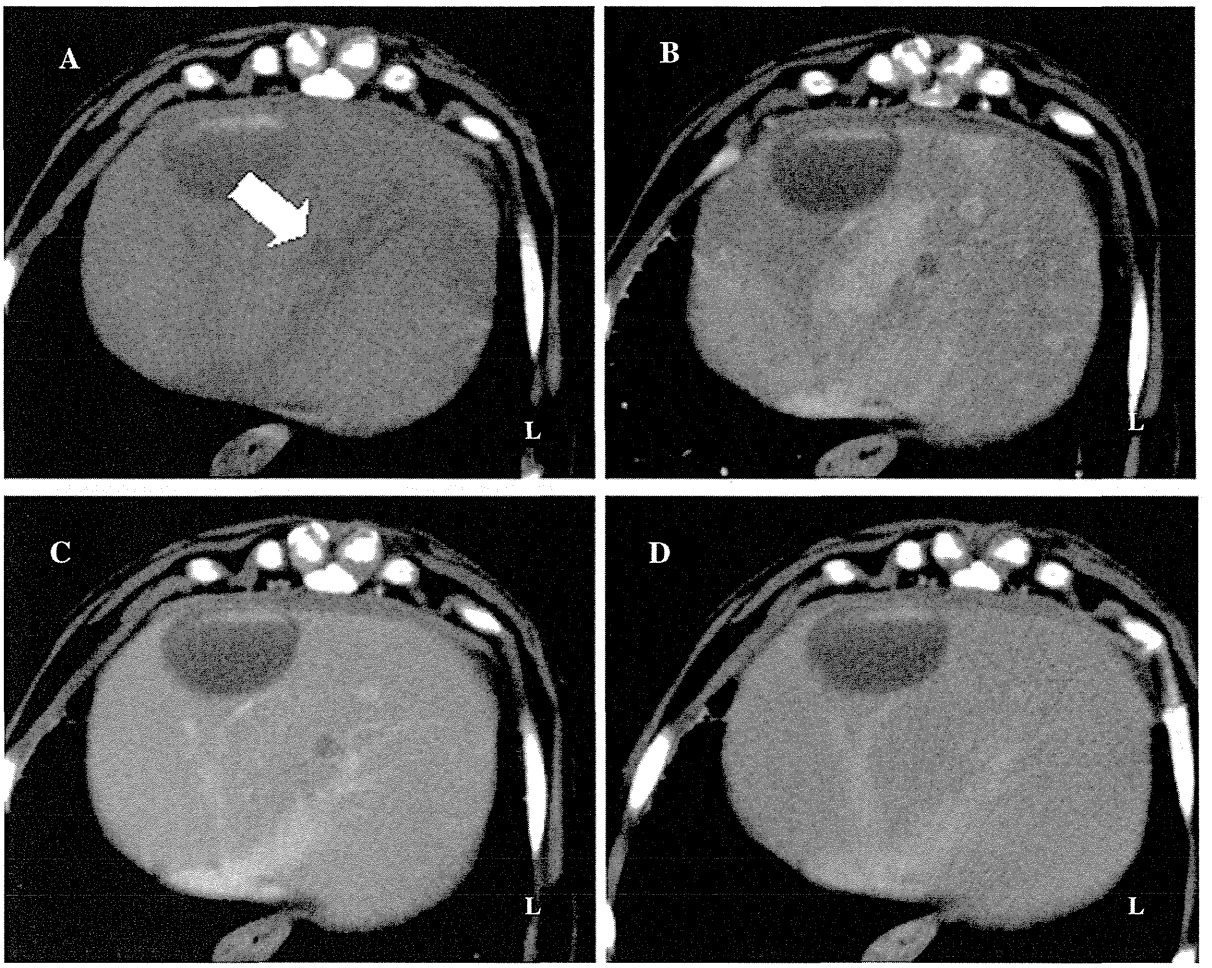

FIG. 6. Triple phase CT characteristics in a dog with a hepatic metastatic tumor. (A) Transverse precontrast CT image showing a mass in the right lobe (arrow). (B) Homogeneous tumor hypoenhancement in the arterial phase. (C) Homogeneous hypoenhancement in the portal venous phase. (D) Homogeneous isoenhancement in the delayed phase. White arrow: tumor

the morphologic characteristics of nodular hyperplasia in dogs closely resemble the histologic architecture of nodular hyperplasia in humans. The homogeneous finding is most likely related to the rarity of hemorrhage and necrosis in nodular hyperplasia in dogs.

In the present study, the most common CT findings in dogs with hepatic metastatic tumors were homogeneous hypoenhancement in the arterial and portal venous phases. A previous study in dogs reported that hypoattenuating lesions within the hepatic parenchyma in postbolus contrast CT (similar to the delayed phase) were probable hepatic metastatic tumors (sensitivity, 73%; specificity, 79%; PPV, 73%).[19] In the delayed phase in our study, 44.4% of the hepatic metastatic tumors showed isoenhancement and 55.6% hypoenhancement. It is suggested that the use of triple-phase helical CT may significantly improve the detection rate of hepatic metastatic tumors.

In conclusion, the most common CT characteristics of hepatocellular carcinoma included a heterogeneous pattern with hyper-, iso-, and hypoenhancement in both arterial and portal venous phases. The most common CT characteristics of nodular hyperplasia were a homogeneous pattern with hyper- and isoenhancement in both the portal venous and delayed phases. The most common CT characteristics of metastatic tumors included a homogeneous hypoenhancement pattern in both the arterial and portal venous phases. Findings from our study indicated that triple-phase helical CT is a useful tool for preoperative differentiation of hepatocellular carcinoma, nodular hyperplasia, and hepatic metastatic tumors based on images in dogs. Large-scale studies are needed in order to determine the diagnostic sensitivity and specificity of triple-phase helical CT characteristics for predicting histopathologic classification of hepatic masses in dogs.

REFERENCES

1. Bluemke DA, Fishman EK. Spinal CT of the liver. AJR 1993;160:787–792.
2. Van Hoe L, Baert AL, Gryspeerdt S, et al. Dual-phase helical CT of the liver: value of an early-phase acquisition in the differential diagnosis of noncystic focal lesions. Am J Radiol 1997;168:1185–1192.
3. Freeny PC, Marks WM. Pattern of contrast enhancement of benign and malignant hepatic neoplasms during bolus dynamic and delayed CT. Radiology 1986;160:613–618.
4. Bonaldi VM, Bret PM, Reinhold C, et al. Helical CT of the liver: value of an early hepatic arterial phase. Radiology 1995;197:357–363.
5. Taniura T, Marukawa K, Yamada K, et al. Differential diagnosis of hepatic tumor-like lesions in dog by using dynamic CT scanning. Hiroshima J Med Sci 2009;58:17–24.
6. Fukushima K, Kanemoto H, Ohno K, et al. CT caharacteristics of praimary hepatic mass lesions in dogs. Vet Radiol Ultrasound 2012;53:252–257.
7. Scialpi M, Volterrani L, Mazzei MA, et al. Small (≤2 cm) atypical hepatic haemangiomas in the non-cirrhotic patient: pattern-based classification scheme for enhancement at triple-phase helical CT. Radiol Med 2009;114:935–47.
8. Akai H, Kiryu S, Matsuda I, et al. Detection of hepatocellular carcinoma by Gd-EOB-DTPA-enhanced liver MRI: comparison with triple phase 64 detector row helical CT. Eur J Radiol 2001;80:310–315.
9. Soyer P, Poccard M, Boudiaf M, et al. Detection of hypovascular hepatic metastases at triple-phase helical CT: sensitivity of phases and comparison with surgical and histopathologic findings. Radiology 2004;231:413–420.
10. Jeon TY, Kim SH, Lim HK, et al. Assessment of triple-phase CT findings for the differentiation of fat-deficient hepatic angiomyolipoma from hepatocellular carcinoma in non-cirrhotic liver. Eur J Radiol 2010;73:801–808.
11. Yamanaka J, Okada T, Saito S, et al. Minimally invasive laparoscopic liver resection: 3D MDCT simulation for preoperative planning. J Hepatobiliary Pancreat Surg 2009;16:808–815.
12. Kutara K, Asano K, Kitagawa M, et al. Evaluation of protocol for abdominal contrast computed tomography in small-breed dogs. J Jpn Vet Med Assoc 2011;64:385–389 (in Japanese).
13. Nakamura K, Takagi S, Sasaki N, et al. Contrast-enhanced ultrasonography for characterization of canine focal liver lesions. Vet Radiol Ultrasound 2010;51:79–85.
14. Kanemoto H, Ohno K, Nakashima K, et al. Characterization of canine focal liver lesions with contrast-enhanced ultrasound using a novel contrast agent-sonazoid. Vet Radiol Ultrasound 2009;50:188–194.
15. Kutara K, Asano K, Kito A, et al. Contrast harmonic imaging of canine hepatic tumors. J Vet Med Sci 2006;68:433–438.
16. Bolog N, Andreisek G, Oancea I, et al. CT and MR imaging of hepatocellular carcinoma. J Gastrointestin Liver Dis 2011;20:181–189.
17. Li CS, Chen RC, Tu HY, et al. Imaging well-differentiated hepatocellular carcinoma with dynamic triple-phase helical computed tomography. Br J Radiol 2006;79:859–865.
18. Tarhan NC, Hatipoğlu T, Ercan E, et al. Correlation of dynamic multidetector CT findings with pathological grades of hepatocellular carcinoma. Diagn Interv Radiol 2011;17:328–333.
19. Irausquin RA, Scavelli TD, Corti L, et al. Comparative evaluation of the liver in dogs with a splenic mass by using ultrasonography and contrast-enhanced computed tomography. Can Vet J 2008;49:46–52.

Evaluation of mRNA expression levels and electrophysiological function of neuron-like cells derived from canine bone marrow stromal cells

Rei Nakano, DVM; Kazuya Edamura, DVM, PhD; Hiroshi Sugiya, DVM, PhD; Takanori Narita, PhD; Ken Okabayashi, DVM, PhD; Tadaaki Moritomo, DVM, PhD; Kenji Teshima, DVM, PhD; Kazushi Asano, DVM, PhD; Tomohiro Nakayama, DVM, PhD

Objective—To investigate the in vitro differentiation of canine bone marrow stromal cells (BMSCs) into functional, mature neurons.

Sample—Bone marrow from 6 adult dogs.

Procedures—BMSCs were isolated from bone marrow and chemically induced to develop into neurons. The morphology of the BMSCs during neuronal induction was monitored, and immunocytochemical analyses for neuron markers were performed after the induction. Real-time PCR methods were used to evaluate the mRNA expression levels of markers for neural stem or progenitor cells, neurons, and ion channels, and western blotting was used to assess the expression of neuronal proteins before and after neuronal induction. The electrophysiological properties of the neuron-like cells induced from canine BMSCs were evaluated with fluorescent dye to monitor Ca^{2+} influx.

Results—Canine BMSCs developed a neuron-like morphology after neuronal induction. Immunocytochemical analysis revealed that these neuron-like cells were positive for neuron markers. After induction, the cells' mRNA expression levels of almost all neuron and ion channel markers increased, and the protein expression levels of nestin and neurofilament-L increased significantly. However, the neuron-like cells derived from canine BMSCs did not have the Ca^{2+} influx characteristic of spiking neurons.

Conclusions and Clinical Relevance—Although canine BMSCs had neuron-like morphological and biochemical properties after induction, they did not develop the electrophysiological characteristics of neurons. Thus, these results have suggested that canine BMSCs could have the capacity to differentiate into a neuronal lineage, but the differentiation protocol used may have been insufficient to induce development into functional neurons. (*Am J Vet Res* 2013;74:1311–1320)

Recently, various types of stem cells have been used in spinal cord regenerative therapy. Several types of such stem cell–based therapies have involved the use of BMSCs for humans, dogs, and other animals because of the abundant availability of BMSCs from adult mammals.[1–4] Bone marrow stromal cells are ideal for transplantation and spinal cord repair because they can be easily isolated, expanded in culture, and delivered.[1] Bone marrow stromal cells are adherent cells found in cultures of bone marrow aspirates, but they are not hematopoietic cells.[4] Bone marrow stromal cells are capable of differentiating into bone, cartilage, fat, and muscle tissues under specific experimental conditions.[5–7]

Results of some studies[8,9] have suggested that BMSCs can differentiate into neurons, astrocytes, and oligodendrocytes. However, the evidence from these studies was inconclusive because their experimental design focused exclusively on the morphological and immunocytochemical properties of BMSC-derived neuron-like cells. For this reason, additional studies that use human or mouse BMSCs have been conducted to determine the mRNA expression levels of neuron markers and the electrophysiological functions of induced BMSCs.

To verify the possible neuronal differentiation of BMSCs, some previous studies[5,7,10–16] have examined

Abbreviations

BHA	Butylated hydroxyanisole
BMSC	Bone marrow stromal cell
DMEM	Dulbecco modified Eagle medium
NSE	Neuron-specific enolase
SOX2	Sex-determining region Y-box 2

Received January 10, 2013.
Accepted May 13, 2013.
From the Laboratory of Veterinary Surgery (Nakano, Edamura, Teshima, Asano), Laboratory of Veterinary Biochemistry (Sugiya, Narita, Okabayashi), Laboratory of Fish Pathology (Moritomo), and Laboratory of Veterinary Radiology (Nakayama), Department of Veterinary Medicine, College of Bioresource Sciences, Nihon University, 1866 Kameino, Fujisawa, Kanagawa 252-0880, Japan.
Supported in part by the Nihon University College of Bioresource Sciences Research Fund for 2009.
Address correspondence to Dr. Edamura (edamura.kazuya@nihon-u.ac.jp).

changes in the mRNA expression of neural stem or progenitor cell and neuron markers before and after the induction of BMSCs into neurons. Investigations that used human or rat BMSCs have demonstrated that mRNA for the neural stem or progenitor cell markers nestin (gene symbol, *NES*) and β III tubulin (gene symbol, *TUBB3*) is present in undifferentiated BMSCs, whereas mRNA for the neuron markers microtubule-associated protein 2 (gene symbol, *MAP2*), neurofilament-L (gene symbol, *NEFL*), neurofilament-M (gene symbol, *NEFM*), neurofilament-H (gene symbol, *NEFH*), and NSE (gene symbol, *ENO2*) is present in neuron-like cells induced from BMSCs.[5,7,10–16]

Furthermore, the electrophysiological function of BMSCs has been investigated, and several studies[13,17,18] have found an increase in the mRNA expression levels of ion channel markers during the neuronal induction of BMSCs. The electrophysiological function of BMSCs after neuronal induction has been examined with calcium imaging and patch clamp recording; the results suggest that human, mouse, and rat BMSCs have the potential to differentiate into functional neurons.[16,18]

A recent clinical trial[3] investigated spinal regenerative therapy with autologous BMSCs in dogs that had paraplegia and loss of nociception in the pelvic limbs. It was reported that 6 of 10 dogs in the transplantation group regained the ability to walk, whereas only 2 of 13 dogs in the control nontransplantation group regained the ability to walk. Furthermore, at the study endpoint, the Texas Spinal Cord Injury Scale scores (a means of assessment of gait, proprioceptive positioning, and nociception) for the transplantation group were significantly higher than those for the control group.[3] Surprisingly, there are very few basic research reports[19–21] on the neuronal differentiation of canine BMSCs, despite the application of canine BMSCs in veterinary medicine. Kamishina et al[19] reported that canine BMSCs develop neuron-like morphological characteristics after induction with dibutyryl cAMP and methyl-isobutyl-xanthine. We previously reported that canine BMSCs had neuron-like morphology and microstructure and were positive for a neuron marker after chemical induction with β-mercaptoethanol and BHA.[20] However, as suggested by Lu et al,[22] the morphological and immunocytochemical changes observed with such methods may be artifacts and may not accurately represent the true potency of BMSCs. On the other hand, Ping et al[23] reported that rat BMSCs induced into neurons with β-mercaptoethanol and BHA were properly epigenetically modified and safe for clinical use. These conflicting interpretations highlight the need for additional investigations of genetic or electrophysiological techniques to clearly understand the neuronal differentiation potency of canine BMSCs.[20,21]

To our knowledge, no study has been conducted to determine the mRNA expression levels and electrophysiological function of canine BMSCs that have been induced into neurons. The purpose of the study reported here was to use molecular biological and electrophysiological techniques to investigate the in vitro differentiation of canine BMSCs into functional, mature neurons.

Materials and Methods

Isolation and culture of canine BMSCs—The study involved 6 healthy Beagles and was conducted with the approval of the Nihon University Animal Care and Use Committee (AP12B015). Each dog was premedicated IV with midazolam hydrochloride[a] (0.2 mg/kg) and butorphanol tartrate[b] (0.2 mg/kg). Anesthesia was induced with an IV injection of propofol[c] (4.0 mg/kg) and maintained with 1.5% to 2.0% isoflurane[d] in 100% oxygen supplied with an endotracheal tube. Before awakening from anesthesia, each dog received another dose of butorphanol tartrate[b] (0.2 mg/kg) IV for pain relief.

Canine BMSCs were isolated in accordance with a method established previously in our laboratory.[20] Briefly, for each dog, 3 mL of canine bone marrow was aspirated from a humerus, and mononuclear cells were separated with density gradient media.[e] Following collection, the mononuclear cells were transferred to a 25-cm^2 plastic culture flask[f] and static-cultured in an incubator at 5% CO_2 and 37°C with α-modified Eagle minimum essential medium[g] and 10% fetal bovine serum.[h] On the fourth day of culture, nonadherent cells were removed when the culture medium was replaced, thereby isolating the canine BMSCs. Canine BMSCs were collected with 0.25% trypsin-EDTA[i] once they achieved approximately 90% confluency.

Neuronal induction of canine BMSCs—After the first passage, canine BMSCs were placed in a 25-cm^2 plastic culture flask at a density of 4,000 cells/cm^2. The BMSCs were then induced into neurons by use of the method described by Woodbury et al.[24] Briefly, after 3 days of culture, the medium was changed to low-glucose DMEM[j] supplemented with 20% fetal bovine serum and 1mM β-mercaptoethanol[k] to induce the neuronal phenotype. After 24 hours of culturing in this medium, differentiation into neurons was induced by transferring the cells to low-glucose DMEM with 2% dimethyl sulfoxide[l] and 200μM BHA.[m] The morphology of these cells was evaluated under an inverted microscope at 2, 4, 6, and 12 hours after the BMSCs were placed in low-glucose DMEM with 2% dimethyl sulfoxide and 200μM BHA.

Immunocytochemical analysis—Canine BMSCs were seeded on 35-mm glass base dishes[n] and cultured for 3 days. After 12 hours of neuronal induction achieved by the method described, the cells were fixed with 4% paraformaldehyde[o] for 15 minutes and processed for immunocytochemical analysis to identify the neuronal differentiation stages. Fixed cells were permeabilized by incubation in 0.2% octylphenol ethylene oxide[p] for 15 minutes at room temperature (approx 22°C). Nonspecific antibody reactions were blocked with serum-free blocking solution.[q] The cells were then incubated for 3 hours at room temperature with primary antibodies, including mouse monoclonal antibodies against rat nestin (Rat-401)[r] to identify a neural stem or progenitor cell marker and mouse monoclonal antibodies against human NSE (clone No. BBS/NC/VI-H14)[s] and against human neurofilament-L protein (clone No. 2F11)[t] to identify neuron markers. After being washed with PBS solution, the cells were

incubated and exposed to goat anti-mouse IgG–conjugated secondary antibody[u] for 1 hour in darkness at room temperature. Cells were also incubated without primary antibodies to control for nonspecific staining by secondary antibodies. Samples of canine spinal cords from 3 adult Beagles that were euthanized for other studies were used as the positive control. These samples were washed 3 times with PBS solution, dried, mounted with antifade reagent,[v] and observed with a confocal laser scanning microscope.[w]

Real-time reverse transcription PCR assay—Total RNAs were extracted from canine BMSCs before and after 6 and 12 hours of neuronal induction by use of a total RNA extraction solution.[x] First-strand cDNA synthesis was performed with 500 ng of total RNA with the aid of a cDNA synthesis kit.[y] Real-time PCR assays were then performed with 2 µL of the first-strand synthesis in a total reaction volume of 20 µL; primers (Appendix) specific for canine neural stem or progenitor cell markers (*NES, TUBB3, and SOX2*), neuron markers (*MAP2, NEFH, NEFL, NEFM, ENO2*, and solute carrier family genes [gene symbols, *SLC1A1, SLC2A3*, and *SLC2A12*]), sodium ion channel markers (gene symbols, *SCN1A, SCN2A*, and *SCN8A*), a calcium ion channel marker (gene symbol, *CACNA1C*), and potassium ion channel markers (gene symbols, *KCNC1* and *KCNA2*), and a 2X mix for real-time PCR applications.[z] The real-time PCR assays of no-template controls were performed with 2 µL of RNase and DNA-free water. In addition, the real-time PCR assays of no-reverse transcription controls were performed with 2 µL of each RNA sample. The PCR assays were conducted with a thermal cycler,[aa] as follows: denaturation at 95°C for 30 seconds, 40 cycles of primer annealing at 95°C for 5 seconds each, and primer extension at 60°C for 30 seconds. The specificity of each primer was verified by a dissociation curve analysis and the direct sequence of each PCR product. The results were analyzed by the second derivative method and the comparative cycle threshold (ΔΔCt) method with the aid of software[bb] for real-time PCR analysis. The amplification of glucuronidase β from the same amount of cDNA was used as an endogenous control, and the amplification of the control group was used as a calibrator sample.

Western blotting—Canine BMSCs before and after 2, 4, 6, and 12 hours of induction into neurons were lysed with a lysis buffer containing 100mM HEPES, 1mM phenylmethanesulfonyl fluoride, and complete mini EDTA-free protease inhibitor mixture[cc] at a pH of 7.4. Canine spinal cord lysate obtained by use of the same lysis solution was used as a positive control. Protein concentrations were adjusted in accordance with the method of Bradford.[25] Extracted proteins were boiled at 95°C for 5 minutes in SDS buffer. Samples containing 5 µg of protein were loaded in each lane of 7.5% polyacrylamide gel[dd] and separated through electrophoresis. Separated proteins were transferred to polyvinylidene difluoride membranes,[ee] treated with blocking solution[ff] for 50 minutes at room temperature, and incubated with the primary antibodies (antibodies against nestin [1:100],[r] neurofilament-L [1:100],[gg] NSE [1:200],[s] and β-actin [1:5,000][hh]) for 120 minutes at room temperature. After washing, the membranes were incubated with horseradish peroxidase–conjugated anti-mouse IgG (1:10,000)[ii] for 90

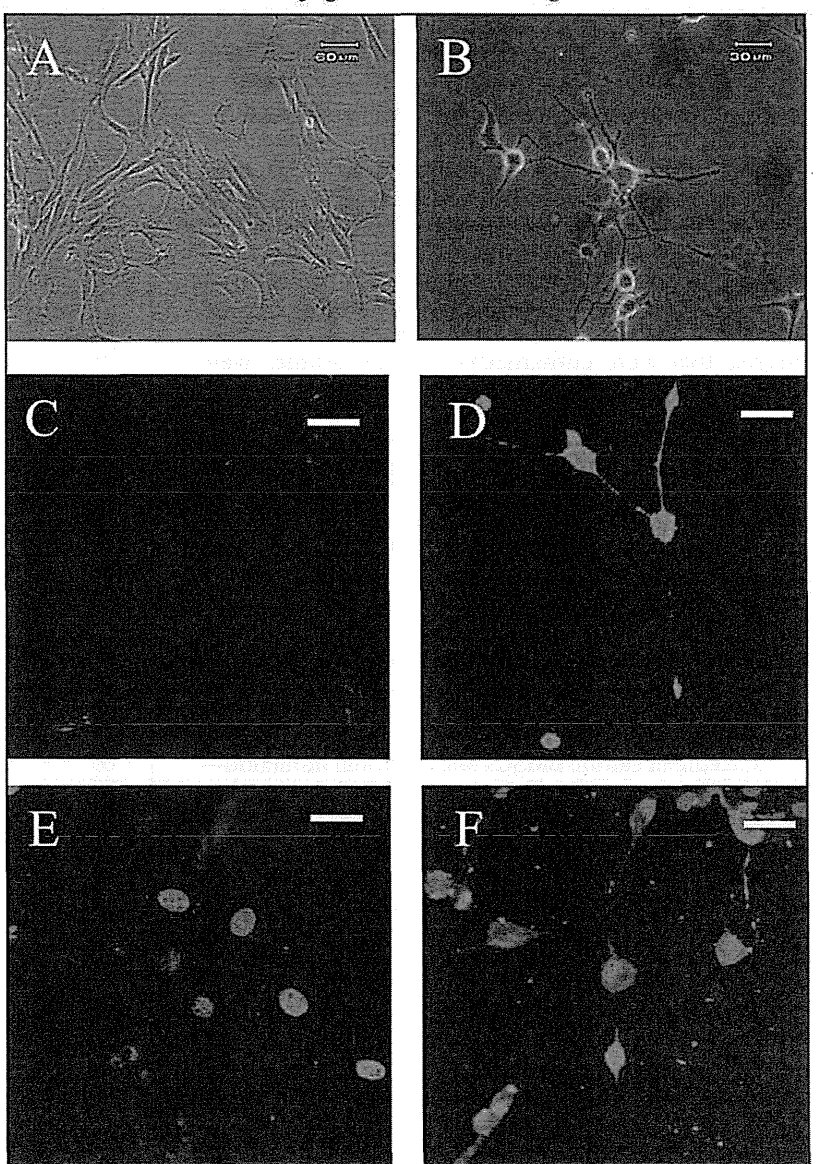

Figure 1—Photomicrographs to illustrate the morphology (A and B) and immunocytochemical staining patterns (C through F) of canine BMSCs before (A, C, and E) and after (B, D, and F) neuronal induction. A large number of canine BMSCs developed neuron-like morphology with multipolar, rounded cell bodies and long, sharp processes after induction (B). Immunohistochemical staining yielded positive results for NSE (D) and neurofilament-L (F) in almost all neuron-like cells. Bar = 60 µm (A) or 30 µm (B, C, D, E, and F)

minutes at room temperature. Immunoreactivity was detected with a western blotting detection reagent.[jj] The chemiluminescent signals of the membranes were measured, and densitometric analyses were performed with a chemiluminescent imager.[kk]

Ca^{2+} imaging—Canine BMSCs (4,000 cells/cm^2) were seeded on 35-mm glass base dishes.[j] Before and after 12 hours of neuronal induction, the cells were incubated in 4.0µM fluorescent dye[ll] to monitor Ca^{2+} influx for 30 minutes in the dark. Following incubation, the cells were washed twice in PBS solution. After washing, the culture medium was changed to Krebs-Ringer-HEPES and bovine serum albumin solution (containing 120mM NaCl, 5mM KCl, 0.96mM NaH_2PO_4, 1mM $MgCl_2$, 11.1mM glucose, 1mM $CaCl_2$, bovine serum albumin [1 mg/mL], and 10mM HEPES; pH, 7.4). The glass base dishes with fluorescent dye–loaded cells were placed at room temperature on the confocal laser scanning microscopy stage.[mm] Fluorescence of the fluorescent dye[ll] was produced by excitation from a 75-W xenon arc lamp with appropriate filter sets (excitation, 488 nm; emission, 527 nm). Each frame in a time-lapse sequence was captured every 2 seconds. After baseline images were acquired, the cells were stimulated with KCl (50mM). The relative changes in intracellular Ca^{2+} concentrations over time were expressed as relative change in baseline fluorescence. Cultured canine neurons derived from 3 adult Beagles that were euthanized for other studies were used as positive controls.

Data analysis—The data are reported as mean ± SE. Statistical analyses were performed with a data analysis software package.[nn] A 2-way ANOVA was performed for comparisons among data obtained before and after 6 and 12 hours of the neuronal induction. A 1-way ANOVA was performed for comparisons between data for canine BMSCs and data for canine spinal cord samples. A Tukey test was used as the post hoc test, and values of $P < 0.05$ were considered significant.

Results

Culture of canine BMSCs and neuronal induction—Before induction, canine BMSCs had fibroblast-like spindle shape morphology (Figure 1). They started to develop neuron-like morphology within 2 hours after the BMSCs were placed in low-glucose DMEM with 2% dimethyl sulfoxide and 200µM BHA, and their morphology continued to change from 2 to 6 hours after the start of induction in a time-dependent manner. However, these changes in morphology ceased by 6 to 12 hours after the start of induction. At 12 hours after the start of induction, the cells had round cell bodies and several long, sharp processes resembling dendrites and axons (Figure 1). Some canine BMSCs detached from the culture flask after 12 hours of induction. There was no difference in neuronal differentiation of canine BMSCs among the 6 dogs.

Immunocytochemical analysis—Almost all canine BMSCs that developed to neuron-like morphology were positive for nestin. In addition, all neuron-like cells derived from canine BMSCs were positive for the neuron markers NSE and neurofilament-L (Figure 1). Strong staining for NSE was evident in cell bodies, whereas neurofilament-L was localized in the cytoplasm, especially at the extremities of the dendrites and axons.

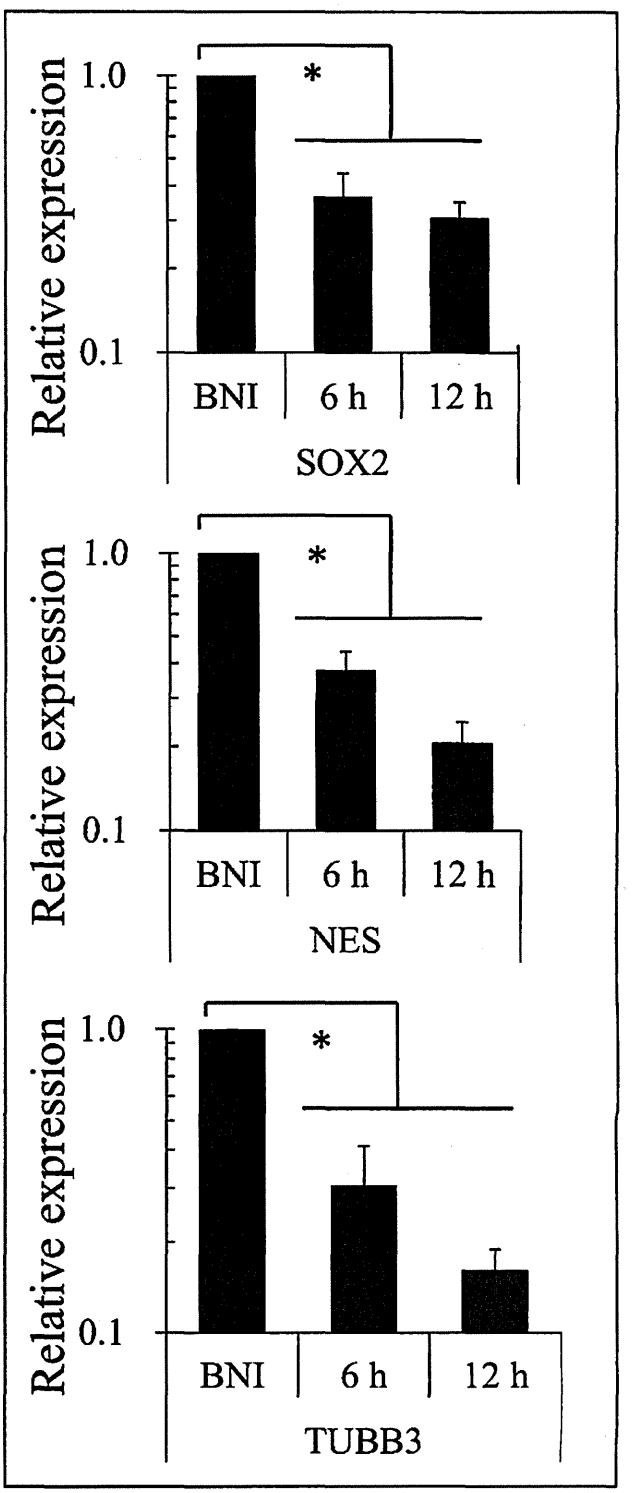

Figure 2—Results (mean ± SE) of quantitative analysis of mRNA expression levels of neural stem or progenitor cell markers (*SOX2*, nestin [*NES*], and β III tubulin [*TUBB3*]) in BMSCs (obtained from 6 dogs) before neuronal induction (BNI) and at 6 and 12 hours after commencement of neuronal induction. The mRNA expression level of each evaluated marker decreased significantly after neuronal induction. *Difference between the BNI value and the other value within the bracket is significant ($P < 0.001$).

mRNA expression levels of markers for neural stem or progenitor cells, neurons, and ion channels—During the induction of canine BMSCs, mRNA expression levels of neural stem or progenitor cell markers such as *SOX2*, *NES*, and *TUBB3* decreased significantly in a time-dependent manner (Figure 2). In contrast, the mRNA expression levels of neuron markers increased after canine BMSCs were induced into neurons (Figure 3). The mRNA expression levels of *MAP2*, *NEFH*, *NEFL*, *SLC1A1*, and *SLC2A3* increased significantly as canine BMSCs were induced into neurons, whereas the mRNA expression levels of the neuron markers *NEFM*, *ENO2*, and *SLC2A12* increased slightly. The mRNA expression levels of *NEFH*, *NEFL*, *NEFM*, *ENO2*, and *SLC1A1* increased until 6 hours of induction but generally decreased thereafter.

The mRNA expression levels of the sodium ion channel markers *SCN1A* and *SCN2A* significantly increased after the induction (Figure 4). However, levels of *SCN8A* mRNA expression did not change significantly. The mRNA expression levels of *CACNA1G* (a calcium ion channel marker) increased significantly during the neuronal induction of canine BMSCs. The mRNA expression levels of the potassium ion channel marker *KCNA2* did not significantly change as a result of neuronal induction, and no fluorescent signals of *KCNC1* were observed before or after neuronal induction.

The mRNA expression levels for almost all neuron markers and several ion channel markers increased after the induction of BMSCs (Figures 3 and 4). The mRNA expression levels of *SCN2A* and *CACNA1G*

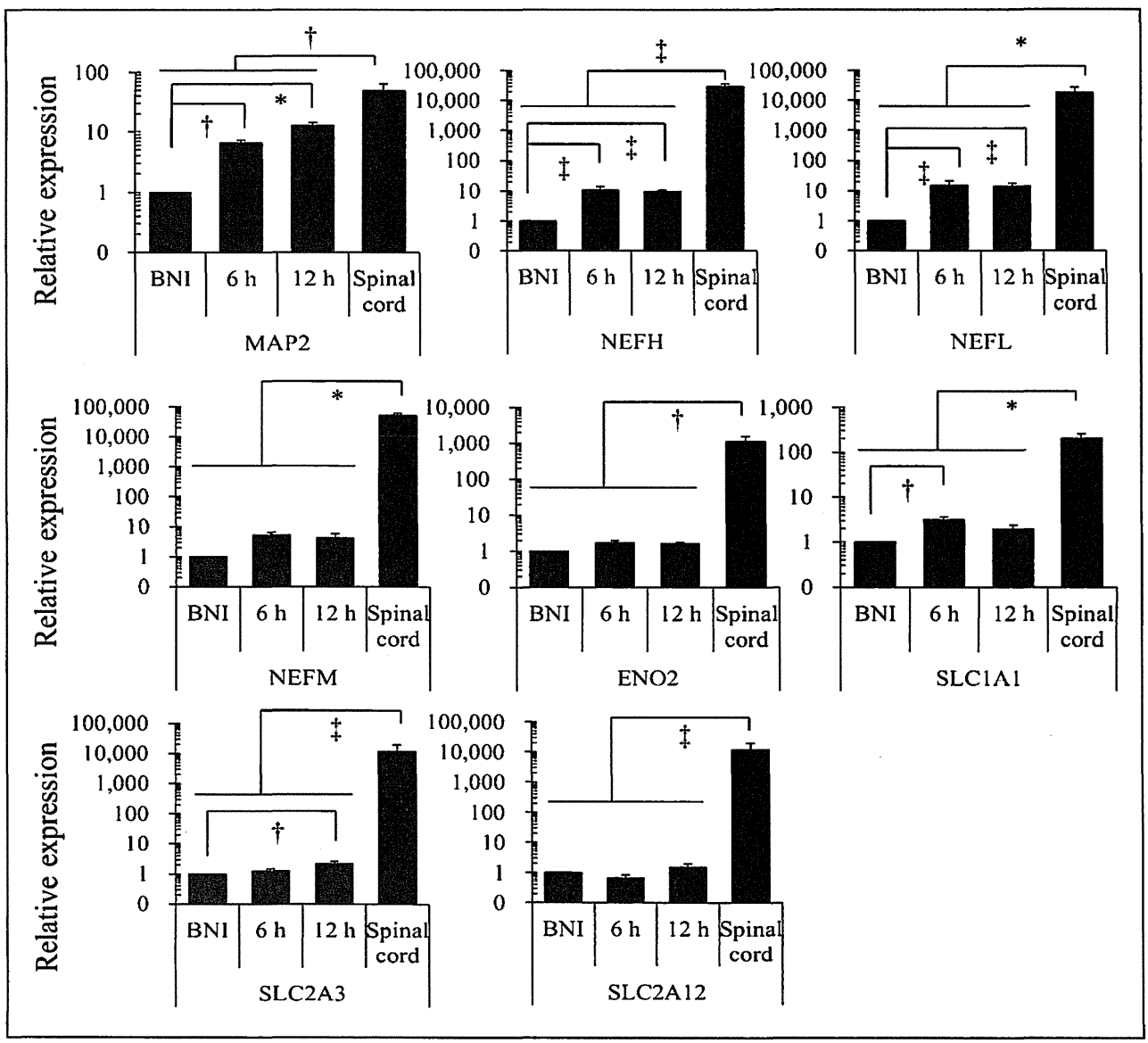

Figure 3—Results (mean ± SE) of quantitative analysis of mRNA expression levels of neuron markers (microtubule-associated protein 2 [*MAP2*], neurofilament-H [*NEFH*], neurofilament-L [*NEFL*], neurofilament-M [*NEFM*], NSE [*ENO2*], and solute carrier genes [*SLC1A1*, *SLC2A3*, and *SLC2A12*]) in BMSCs (obtained from 6 dogs) BNI and at 6 and 12 hours after commencement of neuronal induction and in spinal cord samples obtained from 3 adult Beagles that were euthanized for other studies. All markers increased after neuronal induction. However, the mRNA expression levels of neuron markers in BMSCs did not reach those found in canine spinal cord samples. †Significant ($P < 0.01$) difference between bracketed values. ‡Significant ($P < 0.05$) difference between bracketed values. *See* Figure 2 for remainder of key.

in canine BMSCs after their neuronal induction were equivalent to those in canine spinal cord samples (Figure 4), whereas expressions of other markers did not reach levels comparable to those found in canine spinal cord samples.

Western blotting—Protein expression levels for nestin, neurofilament-L, and NSE increased after the induction (**Figure 5**). Nestin and neurofilament-L expression levels increased significantly until 4 hours after the neuronal induction and then decreased. Neuron-specific enolase protein expression increased, albeit not significantly.

Ca^{2+} influx—Before neuronal induction, intracellular Ca^{2+} concentration in canine BMSCs did not increase in response to KCl stimulation. Similarly, after neuronal induction, intracellular Ca^{2+} concentration in canine BMSCs did not increase in response to KCl stimulation (**Figure 6**).

Discussion

Various types of neuronal differentiation media for BMSCs have been described. Treatment with 2% dimethyl sulfoxide and 200μM BHA is reportedly most effective for neuronal induction of human and rat BMSCs.[20] Therefore, we used media with these constituents to differentiate canine BMSCs into neurons.[24]

In the present study, a large number of canine BMSCs developed neuron-like morphology in a time-dependent manner after chemical induction of neuronal differentiation. Furthermore, immunocytochemical analysis revealed that nearly all neuron-like cells derived from canine BMSCs were positive for neuron markers. These findings are consistent with those of previous studies[16,20,21,24] involving dogs and other animals. Importantly, we observed significant changes in mRNA and protein expression of some neural stem or progenitor cell, neuron, and ion channel markers. However, intracellular Ca^{2+} concentrations in these cells did not increase in response to stimulation with KCl.

Changes in the mRNA expression levels of neuron markers in BMSCs that have differentiated into neurons have been quantitatively investigated by means of real-time PCR assay in several non–dog animal species.[13–15,26,27] However, those studies investigated only a small number of markers and did not examine the time-dependent changes in expression levels. Therefore, in the present study, we quantitatively evaluated the time-dependent changes of 17 markers after the neuronal induction of canine BMSCs.

The mRNA expression levels of all evaluated neural stem or progenitor cell markers significantly decreased during the neuronal induction of canine BMSCs in the present study. Previous studies in humans[13] and chick-

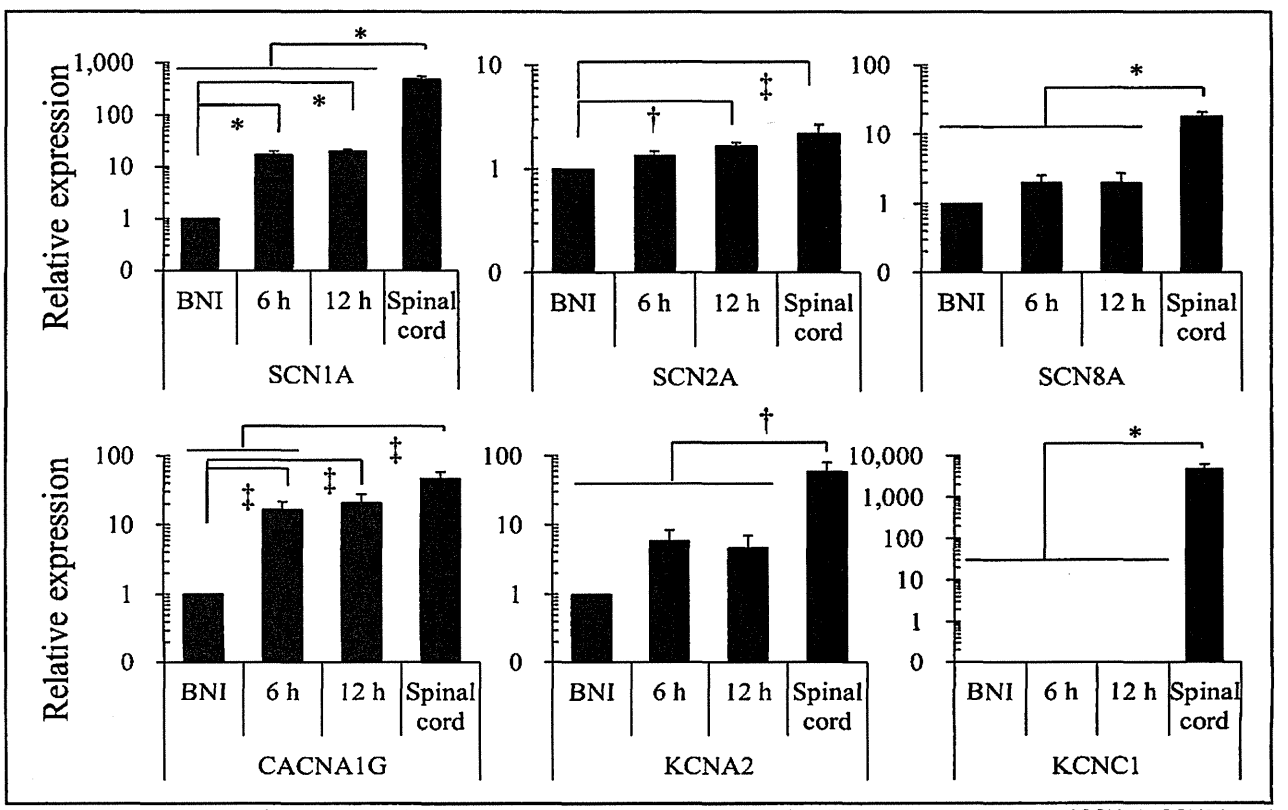

Figure 4—Results (mean ± SE) of quantitative analysis of mRNA expression levels of sodium ion channel markers [*SCN1A*, *SCN2A*, and *SCN8A*]; the calcium ion channel marker [*CACNA1G*]; and potassium ion channel markers [*KCNA2* and *KCNC1*] in BMSCs (obtained from 6 dogs) BNI and at 6 and 12 hours after commencement of neuronal induction and in spinal cord samples obtained from 3 adult Beagles that were euthanized for other studies. The mRNA expression levels of *SCN1A*, *SCN2A*, and *CACNA1G* increased significantly after neuronal induction. However, expression levels of the other markers did not change significantly after induction. The mRNA expression levels of *SCN2A* and *CACNA1G* in canine BMSCs after neuronal induction were equivalent to those in canine spinal cord samples. *See* Figures 2 and 3 for remainder of key.